



Institute of Electrical Measurement and
Measurement Signal Processing
Graz University of Technology



Bachelor's Thesis

Odometry for Wheeled Mobile Robots

Michael Maier

Supervisor: Dipl.-Ing. Dr. Markus Brandner



Mostly Harmless RoboCup Team
Institute for Software Technology,
Graz University of Technology
team@robocup.tugraz.at
<http://www.robocup.tugraz.at>

Graz, July 25, 2012

Contents

1	Introduction	4
1.1	RoboCup	4
1.2	Middle Size League	4
1.3	<i>“Mostly Harmless”</i> RoboCup Team	4
1.4	Odometry	5
1.5	Goals of this Work	6
2	State of the Art in Odometry Measurement	7
2.1	Possible New Odometry Sensors Types	7
2.1.1	Accelerometers	8
2.1.2	Gyroscopes	8
2.1.3	Ultrasonic Doppler Velocimeters	8
2.1.4	Microwave Doppler Velocimeters (Radar)	9
2.1.5	Laser Interferometers	9
2.1.6	Optical Speed Sensors	10
2.1.7	Optical Mice	10
2.2	Current Implementations used in RoboCup	11
2.2.1	<i>“Mostly Harmless”</i> RoboCup Team	11
2.2.2	Other Teams	12
3	Decision for a Type of Odometry Sensor	13
3.1	Requirements for a New Type of Odometry Sensor	13
3.1.1	Current Robot Platform: Krikkit	14
3.1.2	Krikkit3G	16
3.2	Decision	17
4	Sensor Design	21
4.1	Electrical Design	22
4.1.1	ADNS-6010 Laser Mouse Sensor	23
4.1.2	XC164CM Microcontroller	25
4.1.3	Wire-tapping Circuit for Firmware Catch	27
4.1.4	Final Circuit between ADNS and XC	27
4.2	Optical System	30
4.2.1	Optical Path Calculations: Original Mouse Setup	31
4.2.2	Optical Path Calculations: 2-Lens Setup	34
4.2.3	Optical Path Calculations: Telecentric Setup	37
4.2.4	Sensor Mounting and Calibration	39
4.2.5	Lens 2 and Aperture Mounting	42
4.2.6	Illumination	43

4.3	Software	48
4.3.1	Microcontroller-Software	48
4.3.2	PyQt GUI	49
4.3.3	Octave Analysis Scripts	52
5	Experimental Set-Up	53
5.1	Motor and Disk	53
5.2	Reference Speed Sensor	55
5.3	Microcontroller and Host PC	57
6	Experimental Results	58
6.1	Non-telecentric Tests	58
6.2	Telecentric Tests	60
6.2.1	Carpet 1	60
6.2.2	Carpet 2	60
6.2.3	Carpet 3	60
6.2.4	Game Field Lines	62
6.2.5	Second Series of Experiments	65
6.3	Conclusion	66
7	Outlook	68
Bibliography		70

Abstract

In this work, the development of an optical odometry sensor for Middle-Size soccer robots based on a computer mouse for the “*Mostly Harmless*” RoboCup Team is presented.

After summarizing the state of the art, the decision for this particular sensor type is justified. The electrical and optical design of the sensor is described and an introduction into the developed software is given. The documentation given here shall be used for further developments based on this work. A prototype of the sensor is tested on a RoboCup game field simulator. For the experiments, the set-up of the testbed and the workflow of the tests is documented. The experimental results are presented and summarized in a conclusion. The work closes with an outlook to the steps needed for the final implementation on the robots.

Based on this work, a paper named

Parts of these work have been published at the International Instrumentation and Measurement Conference (I²MTC) 2011, located in Hangzhou, China [23].

1 Introduction

1.1 RoboCup

The RoboCup is an international research and education initiative. Its goal is “*By the year 2050, develop a team of fully autonomous robots that can win against the current human soccer world champion team*” [10]. It promotes research in the field of robotics e.g. machine vision, machine learning and autonomous systems. Every year a world championship is accompanied by a conference in a different city around the globe. In addition, various local competitions and conferences are held by local groups.

The RoboCup is split into three divisions: RoboCup Soccer, Rescue and @Home. Every division is split into several leagues targeted at different challenges.

1.2 Middle Size League

In RoboCup Soccer the Middle Size League is most challenging. The robots have to be fully autonomous. All sensors, actuators and computation are on board and no external input is allowed. A team consists of at most 6 robots with a size of max. $50 \times 50 \times 80 \text{ cm}^3$.

The game is played on a field of $12 \times 18 \text{ m}^2$ and lasts 2×15 minutes. The game field surface is generally carpet. The Middle Size League is the only league where an official FIFA ball is used. Objects are distinguished by colour: the game field is green with white lines, robots and referees are black and the ball is red.

The rules are the official FIFA rules [7] with slight adaptations for robotic players. The rules are tightened every year to keep up with the technological progress. For instance the field size has grown from $6 \times 8 \text{ m}^2$ to $12 \times 18 \text{ m}^2$ since the introduction of the Middle Size League.

More than 20 teams from all over the world participate in the Middle Size League, almost all with academic background.

1.3 “*Mostly Harmless*” RoboCup Team

The “*Mostly Harmless*” RoboCup Team participates in the Middle Size League. It was founded at Graz University of Technology at the Institute for Software Technology in 2003. This RoboCup team provides opportunities for master’s, bachelor’s theses and seminar projects. Currently more than 30 students are working on the robots in their free time.

The team regularly participates in European championships as well as World championships. At the RoboCup 2009, which took place in Graz, the team advanced a round in the World Championship for the first time. The third place in the technical challenge was won too.

1.4 Odometry

Odometry is the art of position estimation during wheeled vehicle navigation [26]. The simplest odometry application is the tachometer in a motorcar, where the distance driven is estimated by the rotation count of the wheels. In an omnidirectional wheeled robot the odometry system is more complex as three degrees of freedom (DoF) have to be taken into account. The movement in two directions and the rotational component are represented by the three variables dr , ds and $d\theta$, which are shown in subsection 1.4.

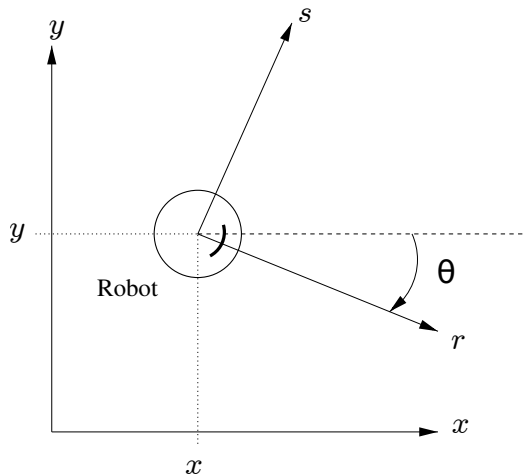


Figure 1: A robot's coordinate Systems [9].

x and y : global robot coordinates

r : forward velocity of the robot in its viewing direction

s : velocity of the robot perpendicular to its front

θ : rotational speed of the robot

In the robot software of the “*Mostly Harmless*” RoboCup Team odometry plays an important role. Together with the vision system and the compass, odometry is a part in the sensor fusion for the parametrization of the world model. Odometry fulfils the following purposes: In the image processing algorithm, odometry data is used as an initialisation vector when comparing two camera frames for calculating the offset between them on updating the robot’s position. Currently, the

camera provides only a frame-rate of 15 Hz and odometry data are available at a higher frequency (50 Hz). Therefore its values are added to the last known position in the world model for the time between two camera frames. At last it acts as a backup system for the mainly vision based localisation system in case of camera blackouts (e.g. blurred images due to the vibrations from a kick or a collision). There are more possible use cases for odometry not implemented yet e.g. anti-slip regulation for every single wheel.

1.5 Goals of this Work

Current odometry systems of the robots measure the rotational speed of the wheels. This has the major disadvantage of the accuracy being limited by the slip of the wheels. The problem is the non-uniform structure of the game field carpet, which has different slip factors in each direction. Due to the special arrangement of the Mecanum wheels (see subsubsection 3.1.1), each wheel has a different speed and angle when driving a straight line. This leads to continuous angular deviations when trying to follow a straight line. The errors accumulate in such a way over time that after 10 m straight distance driven the robot thinks he has turned 90 degrees.

Therefore an wheel-independent odometry system has to be developed. The goals of this work were:

- Gathering requirements for a sensor
- Search for different types of sensors
- Implementation and validation of a prototype

2 State of the Art in Odometry Measurement

When determining the position of a vehicle there are the following options: Relying on absolute, or the relative position measurement from the last known absolute position. The movement of a vehicle can be determined by the difference between absolute position measurements or directly via relative position measurement. Both options rely either on relative or absolute position measurement.

The best known absolute position measurement system is the Global Positioning System GPS. With GPS the position is estimated with triangulation from known reference points, the GPS satellites. This is widely used in robotics for outdoor applications where a GPS signal is available. Indoors other known fixed reference points than satellites can be used. In RoboCup the well-known shape of the soccer field is used for global reference. Without exception every soccer robot uses the features of the game field e.g. the goals, lines and corner posts for orientation.

Another absolute approach for gathering position data is a compass. It also delivers absolute data, but orientation and not position. This approach delivers only one of the three needed degrees of freedom, but it can complete the missing dimension.

For relative position measurement there is the choice to measure distance, velocity or acceleration. Every approach has its advantages depending on the use case. When aiming for the travelled distance it is not wise to measure acceleration, hence the measurement errors would sum up quickly due to the double integration.

The most frequently used odometry systems today are based on the rotational speed of the wheels. The rotary encoders mounted on the axles measure distance. In this work other approaches should be evaluated. These approaches include techniques measuring also velocity or acceleration. Velocity can be measured directly with various implementations based on the Doppler effect e.g. radar or ultrasonic sensors. In the last decade another interesting electronic approach was developed: optical distance metres based on comparing images for translational displacement, as used in optical computer mice.

2.1 Possible New Odometry Sensors Types

In this section technologies to be considered as improved odometry sensor are described in general. The reasons for selecting a particular sensor type for evaluation in this work are explained in section 3.

2.1.1 Accelerometers

Accelerometers consist mainly of flexible mounted masses, which are under the influence of a force. If the mounting consists of springs, the displacement is linear with the applied force. This displacement is then measured. In today's sensors piezoelectric elements are used to convert the force into a signal [4]. In the last years the use of micro electro-mechanical systems (MEMS), where the all mechanical and electrical components are etched in silicon, has been increased significantly. Sensors for three dimensions are now available in tiny package formats. Sensors are either available as professional high-quality finished sensors like the Xsens [5] or as cheap integrated circuits (IC) for consumer applications (like integrated in today's smart-phones). The high accuracy of professional sensors (e.g. the Xsens) comes at a hefty price of € 1.000. The IC-sensors for consumer products are on the other hand still widely inaccurate (in the year 2008).

2.1.2 Gyroscopes

Gyroscopes detect the angular velocity. Historically they consisted of a flywheel mounted in a Cardan suspension. Once spinned up they remain at their orientation, based on the principles of conservation of angular momentum. Due to their nature they are only applicable to one (rotational) dimension, so they must be accomplished with other sensors. Today they are implemented as MEMS similar to the before mentioned accelerometers [31]. Often they are even combined with accelerometers in a single chip package to 6-dimensional sensors.

2.1.3 Ultrasonic Doppler Velocimeters

Ultrasonic Doppler velocimeters work similar as ultrasonic distance sensors. Ultrasonic distance sensors were used in the first robot generation of the “*Mostly Harmless*” RoboCup Team for collision detection.

As with every Doppler measurement, its accuracy is directly dependent of the used wavelengths. At ultrasonic sensors wavelengths around 100 kHz are used. This leads to significantly more accuracy as e.g. Microwave Doppler sensors [12]. When working with ultrasonic sensors on mobile systems, one thing has to be taken into consideration: As with every wave-based system, the relative speed of the medium (air) has to be considerably smaller than the wave speed ($v \ll c$). Through the relatively low velocity of sound, only speeds up to 30 km/h are feasible because of the head wind and turbulences [12].

Additionally, ultrasonic Doppler velocimeters are susceptible to vibrations due to low frequencies [16].

The main use today is in liquid flow measurements.

2.1.4 Microwave Doppler Velocimeters (Radar)

Radar is an umbrella term for object detection systems utilizing electromagnetic waves from 300 MHz up to 3 THz [19]. It can be used to measure the distance of objects and also their speed through the Doppler effect. Depending on the object distance, different wavelength are used. For short-range measurements short-range microwave sensors with 24 GHz are used e.g. radar guns and also for speed measurements on moving vehicles itself [13]. But due to the high frequency they are not so accurate as the before mentioned ultrasonic sensor at low speeds. Another significant drawback are the different reflection rates on different undergrounds (e.g. carpet, wood, concrete and steel) and the underground below the carpet is not known prior to a tournament. Another disadvantage is that radar is disturbed by nearby moving objects.

2.1.5 Laser Interferometers

Speed measurement with laser interferometry is divided into two approaches. One called Laser Doppler velocimetry and the other is referred as Laser Doppler vibrometry.

In Laser Doppler velocimetry, the beam is split into two, one of them directed into the measured volume of flowing liquid. Particles passing through this volume scatter the light with a Doppler shift. The scattered light is received by an optics and interfered with the reference beam on the photodetector. The electrical signal is proportional to the Doppler shift, from which the velocity of the liquid can be determined.

In a Laser Doppler vibrometer the beam is split into two coherent beams. One beam is reflected at an angle at the target and then interfered with the second beam and afterwards collected in a photo diode. The frequency shift between the two beams results in harmonics at the detector [30].

2.1.6 Optical Speed Sensors

The operation of an optical speed sensor is based on comparison of sequentially acquired images from a surface. From the images features are extracted and their position is compared with similar features on the next frame.

Such optical systems are common in industrial and consumer sensors. Exemplary uses are speed sensors for conveyor belts.

The components of an optical speed sensor are usually a high-speed camera acquiring the images from the surface and a Digital Signal Processor (DSP) for analysing the images. In off-the-shelf industrial systems the cameras are usually fixedly mounted and are connected to an external processing device [8].

When the surface contrast is not sufficient to extract enough features for tracking, a little trick helps. Every sufficiently rough surface illuminated with a coherent light source creates a so-called *speckle*. This results from the interference of reflected light waves with different phases due to the roughness of the surface. Therefore illumination with a laser light source increases the contrast a lot on otherwise low contrast surfaces. This is used e.g. in laser speckle strain measurement [29].

When developing such a system from scratch a lot of time and effort is needed. This has been shown by the development of an optical slip-angle sensor [15] for the TUG Racing Team.

2.1.7 Optical Mice

The most common optical speed sensor is used in newer computer mice. Historically computer mice featured a rolling ball with two attached axles (one for each axis), whose rotations are turned into coordinates. In the last 10 years this mechanical principle has been superseded by a strictly electronic approach.

A standard optical mouse consists in a tiny camera taking images of the surface illuminated by an LED. An integrated DSP compares the sequentially acquired images and computes the displacement between them. The sensor outputs movement data to an external microcontroller, which also handles the mouse buttons and translates all data to the USB or PS/2 protocol.

At the time of the search (2008) the fastest gaming mice had a maximum speed of 1.1 m/s. They operate at speeds up to 7000 Hz. Another advantage is their small size and minimal power requirement. Being constructed as an exact gaming device also has disadvantages for RoboCup use: To allow relocating the mouse very fast while lifting off, the best mice used for gaming are designed with a very short working range of only 2 mm.

Laser mice use the same principle as the before mentioned laser speckle sensor.

The only difference to normal mice is the use of a coherent laser source as illumination instead of an LED. The sensor itself remains the same but due to the higher contrast achieved through the speckle they work on more surfaces than common optical mice.

2.2 Current Implementations used in RoboCup

2.2.1 “*Mostly Harmless*” RoboCup Team

The current odometry system of the robots is based on rotary encoders attached to each of the axles. The rotary encoders are needed for motion control and odometry data falls off as a by-product. Data from the rotary encoders are collected by the motion controller, converted into dr , ds , $d\theta$ - coordinate values and send out on the CAN-bus.

Relying on the mechanical contact between the ground and the wheels brings various problems, as already mentioned in subsection 1.5. An effect known from all wheels is the slip occurring by accelerating and braking. The use of Mecanum wheels in a special arrangement (see subsubsection 3.1.1) complicates the relationship between robot and the floor. Due to different speeds and angle of every wheel even when driving a straight line (because the wheels are mounted at around the centre at 120° -steps), every wheel has a different amount of slip. Another factor not to be underestimated is the distinctive direction of the fibre of the carpets [25]. The direction of the fibre results in globally different friction factors in every direction.

A construction error of the power train used in the robots was a loose connection between the gearing box and the motor. The rotary encoders are mounted on the motors and not on the wheels. When the connection between motor and the wheel got loose the rotary encoders delivered only the rotation of the motor and not the distance covered by the wheels. This resulted in complete disorientation of the localisation software during an overrunning motor.

Faulty mechanics are not always responsible for an overrunning motor, it is sufficient when a wheel looses contact with the ground for a moment. This can happen when running aground on a lost screw or other parts lying around the game field or when two robots become wedged together.

For global positioning, in addition to the vision system, a compass is used. Most of the time it worked well, but once in a while we had problems with massive steel girders in the floor below the game field. Due to the over-weighting of unreliable compass data the localisation software got lost completely. Therefore data quality information would be highly appreciated from every sensor used.

2.2.2 Other Teams

Rotary encoders on wheels are widely used e.g. in the team ISocRob [1]. Other teams like IsePorto also accomplish the rotary encoders with a compass [24].

To counter at least the problem with the overrunning wheels when accelerating e.g. the Iranian Team ADRO uses a second set of wheels for measuring odometry data [27].

The use of consumer computer mice in the Middle Size League has been tested by the Milan Robocup Team. They used two optical mice mounted on the bottom of the robot. The main advantages of this approach are the independence of the wheels and the low costs. The availability of more dimensions than needed allows the corrections of non-systematic errors [3].

Accelerometers are used in other leagues e.g. the RoboCup Rescue League or in the Standard Platform League with humanoid robots. They are only used for inertial informations and not for navigation yet [11].

3 Decision for a Type of Odometry Sensor

3.1 Requirements for a New Type of Odometry Sensor

The Middle Size League provides an ideal testbed for mobile robotics. The main demands in robotics are miniaturisation, low cost, energy usage and robustness against the environment. The range of application in the Middle Size League demands the following design parameters for an odometry sensor:

- must deliver linear and rotational accurate data in three degrees of freedom
 - must work on green carpet, other surfaces are bonus
 - must not emit radiation or other disturbing effects irritating other robots or humans
 - resistance against dust from the carpet abrasion
 - shock resistant

The carpet is a particularly hairy concern as its choice is up to the event organizer. The only restriction in the Middle Size League rules and regulations [7] is: green. Therefore the game field surfaces differ in colour and surface roughness at every event. Colours from bright green over dark teal to nearly grey have been seen over the past years. The roughness is another chapter. It ranges from a very even felt with a roughness of maximum 2 mm to an artificial grass like carpet with 15 mm long hairs. Depending on the carpet the robot sinks in some millimetres, which also affects the clearance height.

Three different carpet types are chosen as representative cross-section (see Figure 2). The experiments are made on these carpets types and the sensor has to work flawless on all three samples.

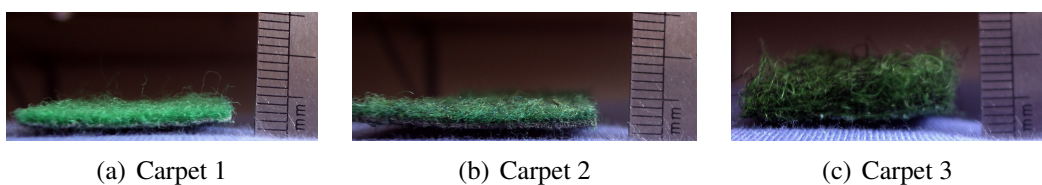


Figure 2: The three different carpet types, on which the sensor must work. The light-green carpet 1 (a) is nearly felt-like with a very smooth surface. Carpet 2 (b) has a mottled teal colour and its hairs are medium long. Carpet 3 (c) has the longest and unevenly hairs and a very dark green colour.

The “*Mostly Harmless*” RoboCup Team requirements for a new odometry sensor are speeds of at least 5 m/s at an operating frequency of at least 50 Hz. From the software side it would be highly appreciated if the sensor delivers data quality information. Data quality information are crucial for the sensor fusion to recognize and de-prioritize erroneous data. The “*Mostly Harmless*” RoboCup Team has bad memories about a malfunctioning compass ruining the world model. At last the “*Mostly Harmless*” RoboCup Team has very tight budgetary limitations depending on external sponsors and due to being a student team. The sensors have to be cheap enough to be affordable for a series of up to six robots.

To get an idea of the field of application of an odometry sensor, the current and next generation of robots of the “*Mostly Harmless*” RoboCup Team are introduced next.

3.1.1 Current Robot Platform: Krikkit

The “Krikkit” robot platform was built in 2006. It was designed solely for playing soccer, in contrast to the old multi-purpose research robot platform. Nearly all components from electronics to mechanical parts were developed in-house. Four robots were build and made their débüt at the World Championship 2006 in Bremen.

Some of the main features of the “Krikkit” robot are shown in Figure 3.

It has a 360° omnidirectional vision system via a firewire-camera pointing upwards to a hyperbolic mirror.

Its brain is a standard mini-ITX industrial PC.

A powerful pneumatic kicker with a 200 bar pressurised air bottle as supply, enables the robot to kick the ball approx. 10 m forward. The kicks are so powerful that the vibrations destroyed the formerly used hard disks which are now replaced by SSD storage. Additionally, every kick caused a camera blackout of nearly 2 seconds due to the vibrations.

Its drive system is also omnidirectional and is based on self-designed Mecanum wheels [25]. The 45°-arrangement of the wheels (see Figure 5) promised smooth and vibration-free operation. The three wheels are arranged in 120°-steps (see Figure 4) and are driven by a 200 W brushless DC motor for each axis. Due to the nature of omni-wheels the robots are able to move in any direction and any orientation.

The motors and all other electric components are supplied by a smart battery system [20] with NiMH rechargeable batteries. All electronic components are connected via CAN-bus.

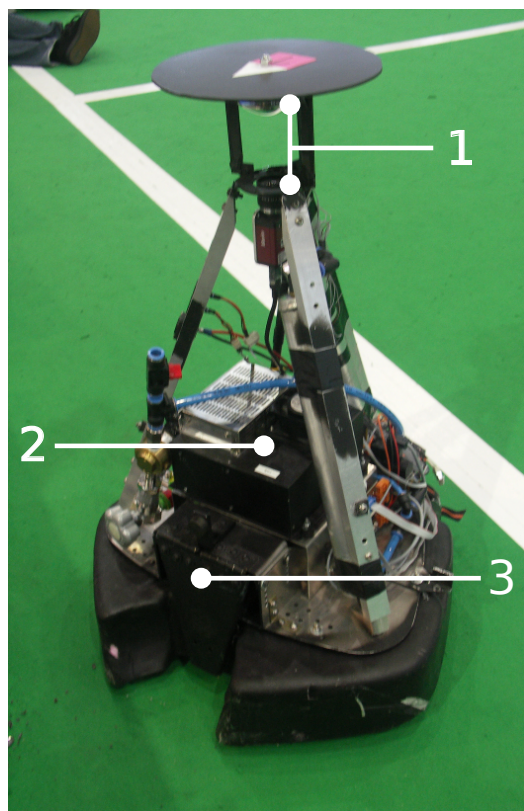


Figure 3: Krikkit robot. Omni-vision with camera and mirror (1); Industrial PC (2); Pneumatic kicker (3); Omni-drive is below the black bumper.

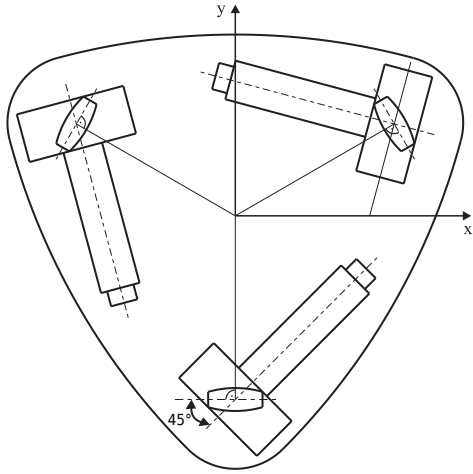


Figure 4: Omni-drive schema of the Krikkit robot. The Mecanum wheels have their 45° small wheels arranged in 120° -steps around the centre. [25]

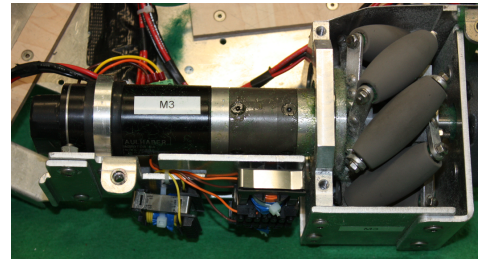


Figure 5: Photo of one of the three Krikkit power trains, visible are from left to right: Motor, gearbox and Mecanum wheel.

The Krikkit robots served well for four years and much was learned. Before RoboCup 2009 in Graz a major mechanics overhaul was done. In the meantime all major electronic components also reached the end of their life cycle. With the knowledge gained, the successor of the Krikkit generation is in development now.

3.1.2 Krikkit3G

The next generation of robots is in development since mid-2010. It will be a direct successor of the Krikkit generation, therefore the name *Krikkit3G*.

The successful concepts are adopted nearly unchanged:

- omnidirectional drive with the three Mecanum Wheels
- omni-vision system
- pneumatic kicking concept
- use of a standard mini-ITX industrial PC
- modularity of all components

The new robot design focusses on the strict modularity of all components. It has been shown that fast disassembling and replacing of critical components is crucial in the fast-paced tournament environment. The power train has especially been

modularised. The wheel, gearing, motor and motor electronics can be swapped as a whole group.

Tests showed that the smoothness of the Mecanum wheels were insufficient due to manufacturing imprecision. The resulting vibrations should be filtered out by an independent wheel suspension. The independent wheel suspension adds an operating range of ± 10 mm to the clearance height of 20 mm.

For the kicking system the pneumatic principle was kept, but it is now much more versatile. It can switch between high and flat kicks at full power and side-kicks are also possible now. Featuring a new ball guidance system allows grabbing the ball for a short moment. This feature becomes especially useful when decelerating with the ball. The vibrations from the kicker, disturbing the camera, should also be reduced by an active final position dampening system. Nevertheless short disturbances in the vision system, due to the vibrations, will remain during the kicks.

Big changes have been made in the electronic sector. A new microcontroller core (An ARM Cortex M3) is used on every component, which replaces the different microcontroller architectures used before. The smart battery system also got a major upgrade featuring even smarter batteries. As power supply only two DC lines with 24 V and 7 V are available, with the 7 V-line being limited to ≈ 5 A. Odometry data must be output on the robot's CAN-bus.

In the mechanical design of the Krikkit3G robots space is now also provided for an improved odometry system (see Figure 6), which will be developed based on this work. The available space for each of the three proposed odometry sensor mount points is limited to $50 \times 50 \times 110$ mm³.

3.2 Decision

The focus lies on cheap consumer-grade sensor based solutions, due to the hefty price for industrial sensors. Advantages of industrial solutions would be their robustness and in most cases their native CAN-bus interface. The big disadvantages of industrial sensors are their size, weight and power requirements. Finished industrial radars, laser interferometers and optical speeds sensors mostly use 230 V AC and require an external processing unit and are simply too big and heavy for middle size robots [6, 8, 13].

The possible odometry sensors introduced in subsection 2.1 are evaluated by means of the requirements. The results are summarized in Table 1.

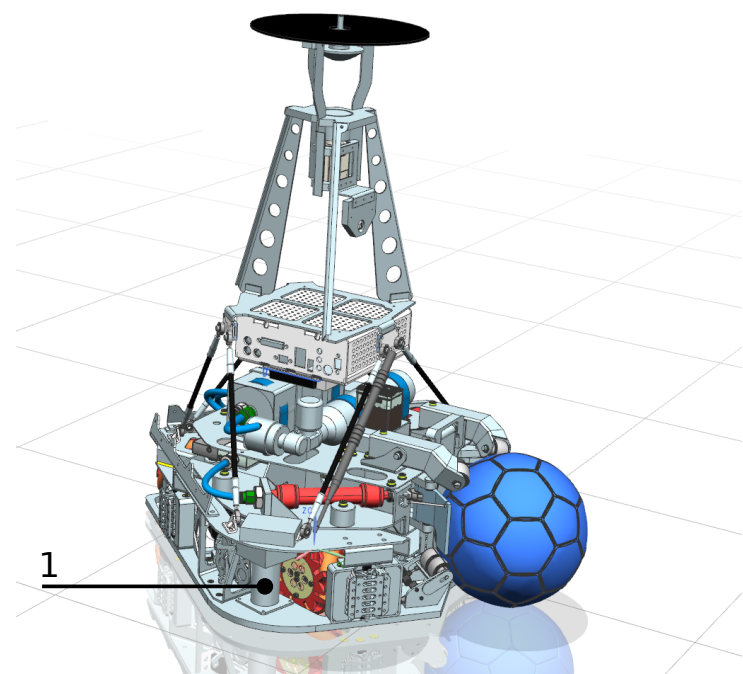


Figure 6: Rendering of the currently in construction Krikkit3G robot (Without outer hull). (1) indicates the position of one of the three proposed odometry sensor mount points.

	<i>Acc./Gyro. high-end</i>	<i>Acc./Gyro. consumer</i>	<i>Ultrasonic</i>	<i>Radar</i>	<i>Laser interferometer</i>	<i>Custom Optical</i>	<i>Consumer Mice</i>
Cost	5	1	2	2	2	5 ⁴	1
Size	2	1	3	4	2	5	1
Power	2	1	2	4	2	4	1
Speed	1	2	5 ¹	4	1	1	4
Surface Distance	-	-	4	4	1	2	3
Surface Type	-	-	4	5 ³	1	1	1
Accuracy	2	5	2	4	1	1	1
Environmental Influence	2	4	5 ²	5	1	1	1

¹ Wind speed and turbulences affect the wave carrier medium air.

² Reflections are a problem and we must use at least 3 sensors in close proximity to each other.

³ Different undergrounds (e.g. carpet, wood, concrete and steel) have very different reflection rates and the underground below the carpet is not known prior to a tournament.

⁴ The components involving the camera and the needed FPGA-processor would be unaffordable for even one robot [15].

Table 1: Sensor-Types and their score on the requirements. Lower numbers score better, with 1 best and 5 the worst, being a knock-out criteria.

When looking at Table 1 only two types of sensors remain possible. The use of custom-build laser interferometers, especially vibrometers, was considered. The Institute of Electrical Measurement and Measurement Signal Processing does some work in this field. The approach seemed promising but was not followed due to lack of time.

Mouse sensors were considered most promising from the start of this project. They are cheap and fit into the size and power requirements of a middle size robot. The disadvantages of missing range and maximum speed can be negated by replacing their optics. By adding more magnification and setting the focus plane farther away from the sensor, maximum speed and range could be extended. With the use of two sensors the needed three degrees of freedom can be reached with extra redundancy.

The “*Mostly Harmless*” RoboCup Team requires odometry data delivered on the CAN-bus, not the mice’s native USB. To convert four dimensions of data from two sensors into the needed dr , ds , $d\theta$ - values on the CAN-bus, a microcontroller controlling the two mice sensors is mandatory.

4 Sensor Design

The task is the following: Develop an odometry sensor from a given mouse sensor. At the beginning of this project we got a prototype sensor sponsored from the German RoboCup Team Carpe Noctem¹.

It consisted of a mechanically modified Razor Copperhead laser mouse. In this mouse type a sensor from Avago Technologies is used, the ADNS-6010. The sensor and illumination were dismounted from its printed circuit board (PCB) and relocated in a new casing because of mechanical size constraints (see Figure 7). It was reconnected to its PCB via thin enamelled copper wires. It still worked although the recommended distance to some circuit elements was exceeded considerably due to the 'extension' of the IC pins.

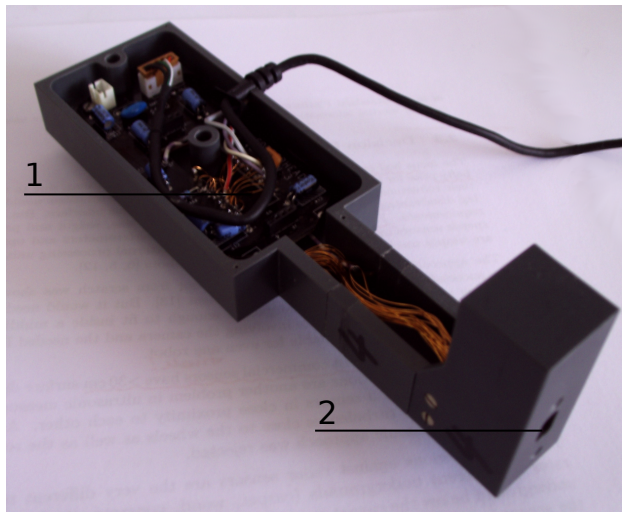


Figure 7: Prototype sensor from the German RoboCup team Carpe Noctem. The Sensor IC and the illumination was relocated from the PCB (1) to an extension mount (2).

Two modifications were to make: Providing a CAN interface instead of USB and creating a new optics system. For the new optics system, access to raw sensor image data was needed for focussing the system. Reading out raw image data was not possible via the mouse's USB interface, only directly via the SPI (Serial Port Interface) of the sensor chip. Therefore it was chosen to remove the sensor chip from the mouse and connect it directly to an external microcontroller. This kills two birds with one stone. The microcontroller can provide a CAN-bus interface

¹<http://carpenoctem.das-lab.net/> (last accessed 10.02.2010)

and provides direct access to the sensor.

For evaluation a serial port (RS-232) is used instead of the CAN bus because of its simpler nature. In summary, we had to create a system as shown in Figure 8.

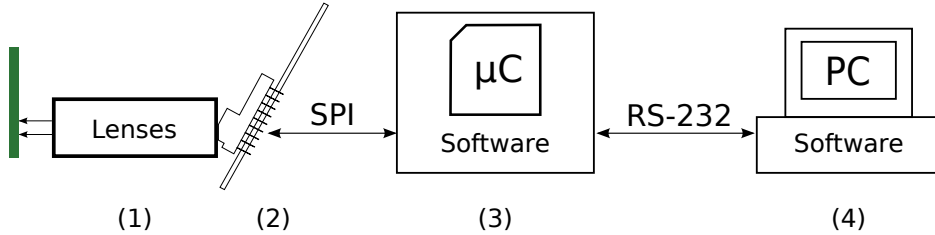


Figure 8: Schemata of the developed evaluation sensor. From left to right: Optical system (1) attached to the mouse sensor, custom PCB (2) with the mouse sensor connected via SPI to microcontroller (3), which is itself connected to a host PC (4) via serial port (RS-232). The low level part of the software runs on the microcontroller and the user interface runs on the host PC.

We used an Infineon XC164-CM microcontroller evaluation board [17] of which several are available in the “*Mostly Harmless*” RoboCup Team. For the mouse sensor a custom PCB with minimal needed circuit and the needed connections to the microcontroller was designed. The electronics part of this work is described in subsection 4.1.

The Software part is split into low-level communication with the mouse sensor running on the microcontroller and the controlling and visualising part on the host PC, see subsection 4.3.

The optical changes of the system concerning design and implementation are described in subsection 4.2.

4.1 Electrical Design

The ADNS-6010 laser mouse sensor runs on custom firmware, which must be flashed from the microcontroller to the sensor before motion read is possible. Due to reluctant support from Avago Technologies, the firmware was not available as binary. Therefore two stages for connecting the microcontroller board with the ADNS-6010 were needed.

The first stage features the microcontroller wire-tapping on the SPI channel between the original mouse microcontroller and the sensor, monitoring the communication and recording the firmware as it is flashed on the sensor.

Now that we have the firmware the sensor is unsoldered from the mouse PCB and inserted in a custom PCB with minimal needed circuit for communication with

the new microcontroller.

In this subsection the ADNS-6010 laser mouse sensor is introduced at first. Then the XC164CM microcontroller and its development board are presented. At last the needed circuit between the two chips for each stage is shown.

4.1.1 ADNS-6010 Laser Mouse Sensor

The ADNS-6010 laser mouse sensor measures changes in position by optically acquiring sequential images and mathematically determining the direction and magnitude of movement. It contains an image acquisition system, a Digital Signal Processor (DSP) and a four wire serial port. It acquires microscopic surface images via the lens and illumination system. These images are processed by the DSP to determine the direction and distance of motion. The DSP calculates the Δx and Δy relative displacement values. The Δx and Δy values are output on the serial port to an external microcontroller [2].

It features the following specifications:

- High speed motion detection - up to 1100 mm/s and 20 g
- Programmable or automatic frame rate over 7080 frames per second
- 400, 800, 1600 or 2000 cpi selectable resolution
- Single 3.3 V power supply
- Four-wire serial port along with power down and Reset pins
- Integrated laser driver controller for illumination laser diode

It comes in a 20-pin package bundled with its own lens and matching vertical-cavity surface-emitting laser diode (VCSEL). It uses 3.3 V, but can be connected to a 5 V-microcontroller without level shifting techniques needed. The data connection to the microcontroller is a four-wire serial port interface (SPI). The lines are source clock (SCLK) and chip select input (NCS) which activates the SPI and the in (MOSI, Master Out/Slave In) and out (MISO, Master In/Slave Out) data lines. The microcontroller acts as master and always initiates the data transfer. Some additional circuit e.g. external reference capacitors and a resonator is needed as shown in Figure 9.

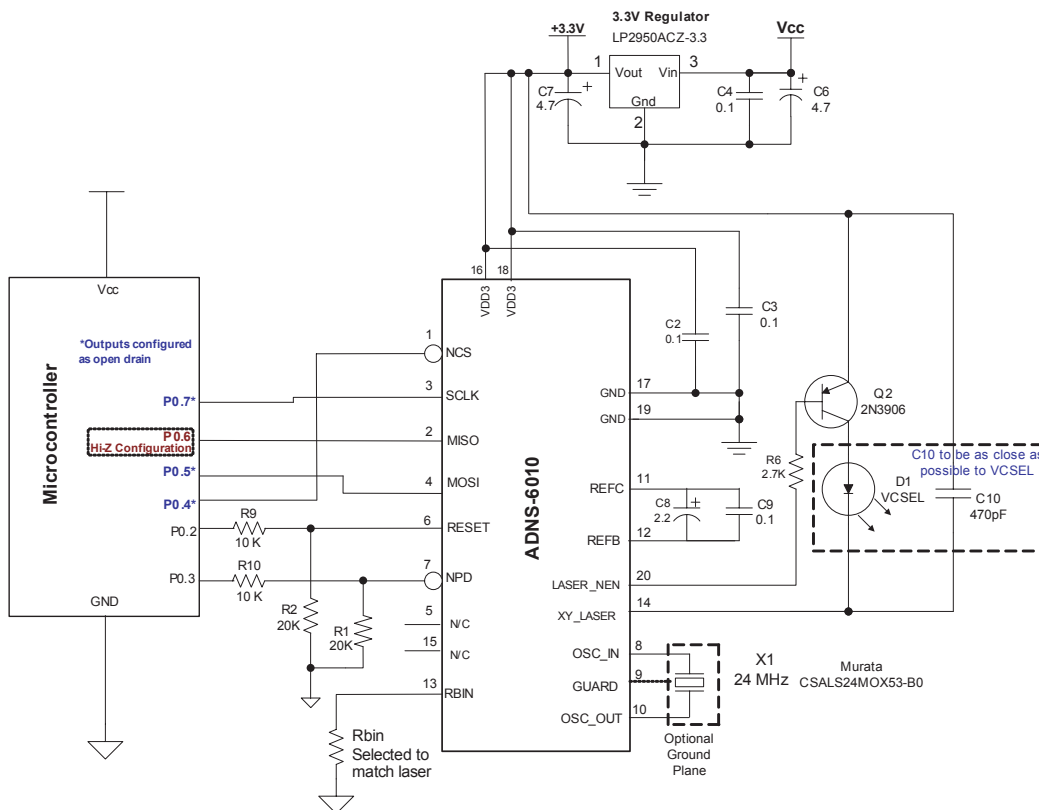


Figure 9: Minimal circuit for the ADNS-6010 laser mouse sensor recommended from data sheet [2]. The ADNS-6010 is in the centre, the external microcontroller on the left side, the VCSEL laser and driver on the right. The 3.3 V-regulator needed on 5 V supply is on top of the diagram.

4.1.2 XC164CM Microcontroller

The XC164CM microcontroller comes from the Infineon XC166 family, as used in the Krikkit robots for motion control [21]. It is a 16-bit microcontroller, which allows convenient programming via the Keil² IDE.

A XC164 development board [17] as seen in Figure 10 is used. It has all pins of the XC core easily accessible and all needed circuit for the XC is on board. The XC164 on the board runs on 5 V supply, which is tapped to power the ADNS-6010. The use of an oversized evaluation board is of course no option for the Krikkit/3G robots, but sufficient for our experiments.



Figure 10: XC164CM development board [17] used to control the sensor. It needs 12 V external power supply (connector visible on the bottom). It has external RS-232 (left) and CAN (middle) connectors.

For the experiments the microcontroller board is connected via its serial port (RS-232) to a host computer. Programming as well as controlling and reading out data is done over the serial port. The CAN interface of the microcontroller is only needed on the final implementation on the robot, therefore it is not connected during the experiments.

For connection to the ADNS-6010, a 10-pin header is soldered subsequently on the development board and connected to the needed pins of the XC core (see Figure 11). Besides the 4-port SPI, reset and power down (NPD) lines and the power supply (VCC and GND) are intended for the ADNS-6010. Then it is connected via a ribbon cable to the original mouse PCB for wire-tapping (Stage 1) and later to the new ADNS sensor board (Stage 2). The pin-assignment of the header and cable can be seen in Table 2.

²Keil uVision3 V3.30a © Keil Software Inc. downloadable from: <http://www.keil.com> (last accessed 26.05.2011)

Pin	Name	XC Port	PCB Con
1	NCS	P3.6	X107.1
2	MISO	P3.8	X107.3
3	SCLK	P3.13	X107.7
4	RESET	P9.4	X107.15
5	MOSI	P3.9	X107.4
6	N/C	-	-
7	NPD	P9.5	X107.16
8	N/C	-	-
9	GND	-	X107.9
10	VCC	-	X107.8

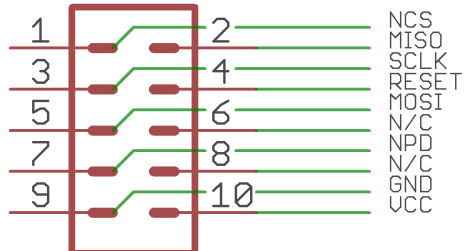


Table 2: Pin-assignment of the 10-pin header and cable on the XC164CM development board.

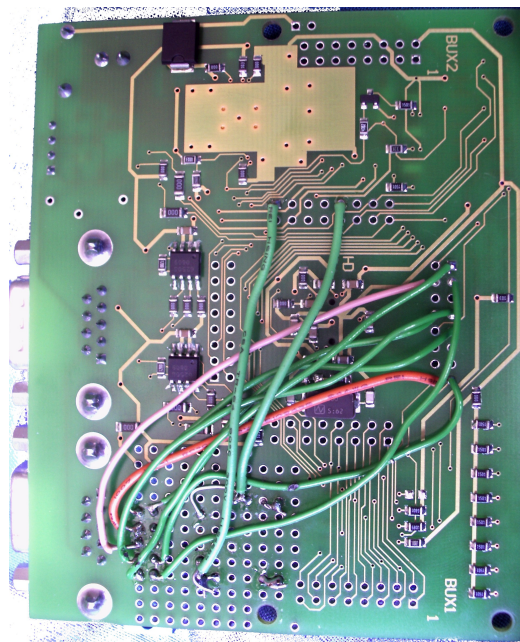


Figure 11: Wiring of the XC164CM development board. The pins from the XC are connected from the header X107 (middle right) to the 10-pin header (lower left) and from the header X106 (top) to the measurement bridge (bottom).

The second role of the XC board is the reference speed measurement on the experimental set-up via a light barrier. The circuit and function of the needed measurement bridge is described in subsection 5.2

4.1.3 Wire-tapping Circuit for Firmware Catch

The goal in stage 1 is to catch the firmware written from the mouse microcontroller to the ADNS-6010 for our use. The firmware must be flashed after powering up the mouse to the ADNS-6010. After powering up, the reset pin of the ADNS-6010 is toggled by the mouse microcontroller and directly after that event the control sequence for downloading to the SROM starts followed by the firmware. The idea is to connect the XC as a second slave to the bus and record all communication between the mouse microcontroller and the ADNS from the moment the reset pin is toggled. We only need four lines: GND, RESET and from the data interface only SCLK and MOSI. The SCLK is needed because SPI works as a synchronous interface and we do not know the exact frequency of operation. We only need the data written from the microcontroller to the ADNS (MOSI), the reverse channel is uninteresting.

In the implementation four wires are soldered on the GND, RESET, SCLK and MOSI pins of the mouse and connected via a crimp plug (pin assignment see Table 2) to the 10-pin header on the microcontroller development board. This set-up can be seen in Figure 12.

4.1.4 Final Circuit between ADNS and XC

After successfully saving the firmware in stage 1 we were able to connect the ADNS-6010 directly to our microcontroller. With the outputs of the XC164CM configured as open drain, we connected the 5 V microcontroller with minimal circuit to the 3.3 V ADNS-6010. The ADNS-6010 is mounted on a custom PCB with the following features: 10-pin header for connection to the microcontroller board, 3.3 V-regulator, circuit needed for the VCSEL diode, resonator and reference capacitors.

The board layout is designed in the Cadsoft EAGLE³ Software. The EAGLE-files are available in the AFS⁴. The circuit and board layout for the PCB can be seen in Figure 13 and Figure 14.

³EAGLE light edition v5.10.0 © CadSoft, <http://www.cadsoft.de> (last accessed 01.01.2011)

⁴/afs/robocup.tugraz.at/electrics/design/99_concepts/adns_testplatine/v1.1 (last accessed 21.12.2010)

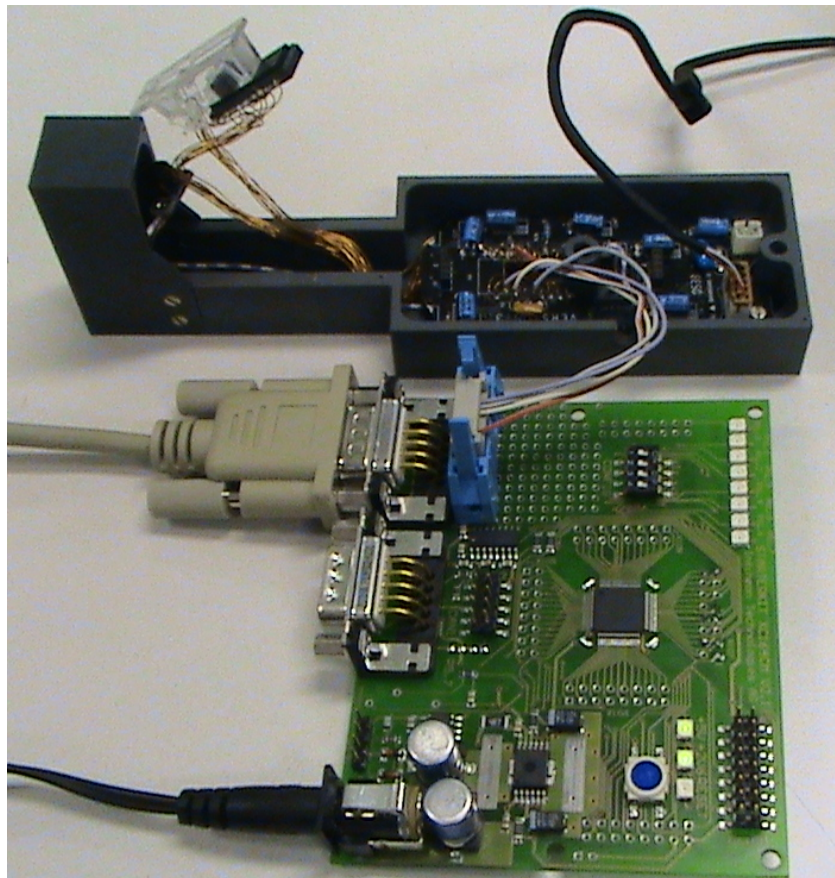


Figure 12: Implementation of the wire-tapping to catch the firmware (stage 1). On top is the mouse with the sensor on its original PCB. The four needed lines GND, RESET, SCLK and MOSI are connected to the microcontroller development board (bottom). Our microcontroller is configured as slave and waits for the reset signal after which the communication between mouse microcontroller and ADNS on the SPI is monitored and the firmware recorded.

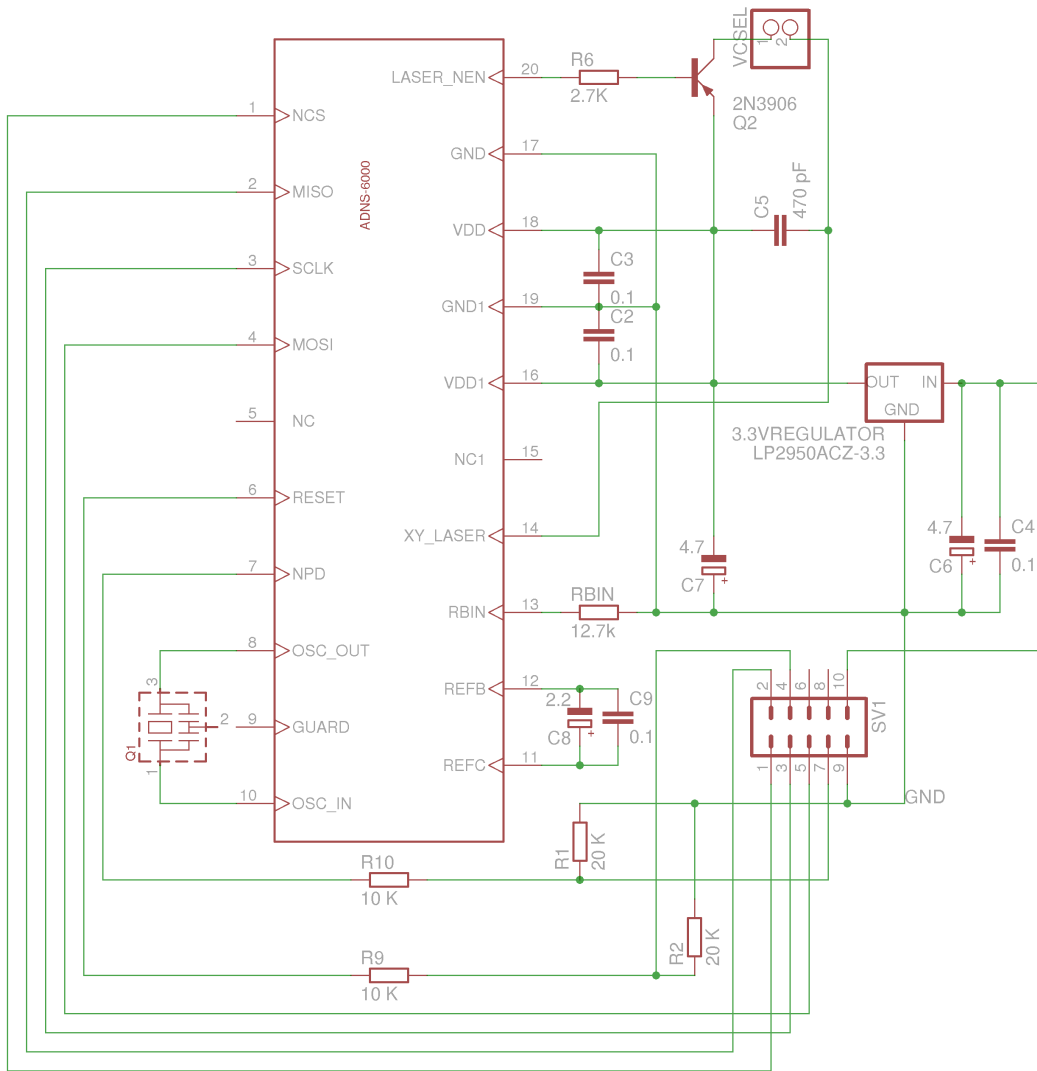


Figure 13: Circuit for the custom PCB for the ADNS-6010 laser mouse sensor. In the lower right is the 10-pin header for the connection to the microcontroller board. In the right middle the 3.3 V-regulator which takes it power from the 5 V-line from the microcontroller. Top right is the header for the externally connected laser diode.

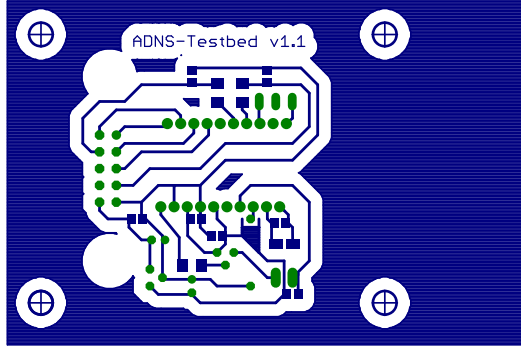


Figure 14: Board layout for the custom PCB for the ADNS-6010 laser mouse sensor. The 20-pin sensor is in the middle. On the left is the 10-pin header for the connection to the microcontroller board. Below the sensor is the 3.3 V-regulator and driver and header for the externally connected laser diode. Sketch not to scale.

4.2 Optical System

The optical properties of the mouse have to be improved by an appropriate optical system. The most important drawback of the ADNS-6010 is its maximum capable speed of 1.1 m/s, it must be improved to 5 m/s. The maximum speed is linear dependent on the field of view of the sensor. Magnifying the field of view of the sensor by five times will also increase the maximum speed to over 5 m/s.

Another wished feature is a distance to the surface from at least 20 mm. The ADNS-6010 with its original lens has only 2 mm clearance height, this has to be improved.

Due to varying clearance height resulting from the new independent wheel suspension as well as different carpets, the dependency of the magnification from the clearance height should be eliminated. This can be achieved by a telecentric system [28].

It is chosen to keep the original lens in its position and extend the optical system with additional lenses. At first, a lens is added in front of the original lens, which provides the needed magnification. Then, a second lens is added responsible for the telecentric set-up. We call the original mouse lens L_1 , the magnification lens L_2 and the telecentric lens L_3 . The aperture stop of the system responsible for the sharpness of the image is placed at L_2 . The whole optical system can be seen in Figure 15.

The optical system with the sensor is built using a Linos 40 mm micro-bench carrier system [22] which allows easy adjustment of all optical components. For L_2 and the aperture a custom mount, based on micro-bench carriers, has to be

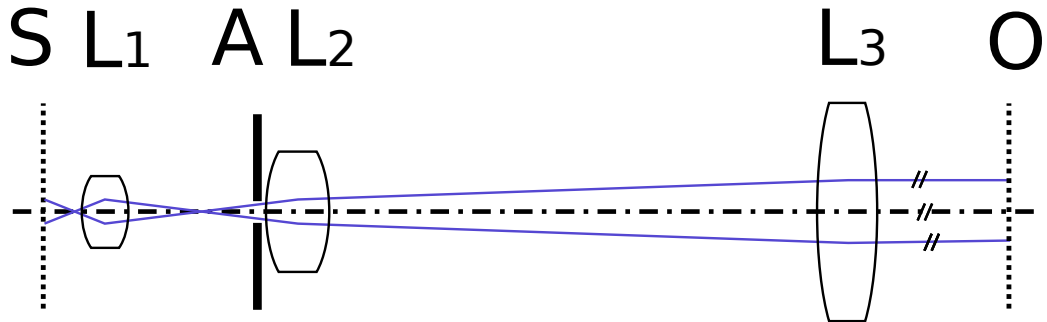


Figure 15: Complete optical system: Image plane S on the left side, original mouse lens L_1 , aperture stop A, magnification lens L_2 , telecentric lens L_3 and object O on the right side.

developed due to space constrains (see subsubsection 4.2.5). The mount of the sensor itself on the micro-bench carrier is described in subsubsection 4.2.4.

The calculations involved figuring out the original mouse optical system, designing the second lens and needed aperture and choosing an appropriate lens for the telecentric set-up. All calculations are verified with WinLens3D⁵ and are available in the AFS⁶. Detailed explanations of the calculations follow now.

4.2.1 Optical Path Calculations: Original Mouse Setup

To alter the properties of an optical system by expansion with more optical elements the optical properties of the base system must be known. The original mouse sensor set-up consists of the sensor, the lenses for the sensor and the VCSEL combined as one plastic part and the VCSEL (see Figure 16). The exact parameters of the optical system are not specified in the data sheet. They have to be estimated based on retroactive measurements and own observations. From the data sheet [2] the following properties are known:

- Distance of sensor plane to lens plane is 5.88 mm.
- Distance from lens plane to object plane is also 5.88 mm.
- The lens material has a refraction index of $n = 1.5713$ at $\lambda = 842 \text{ nm}$.
- Lens thickness is 2.43 mm.

⁵Qioptiq Photonics GmbH & Co. KG, WinLens3D Basic V1.1.11, <http://www.winlens.de> (last accessed 30.12.2010)

⁶/afs/robocup.tugraz.at/projects/2010_improved-odometry/lenses/ (last accessed 30.12.2010)

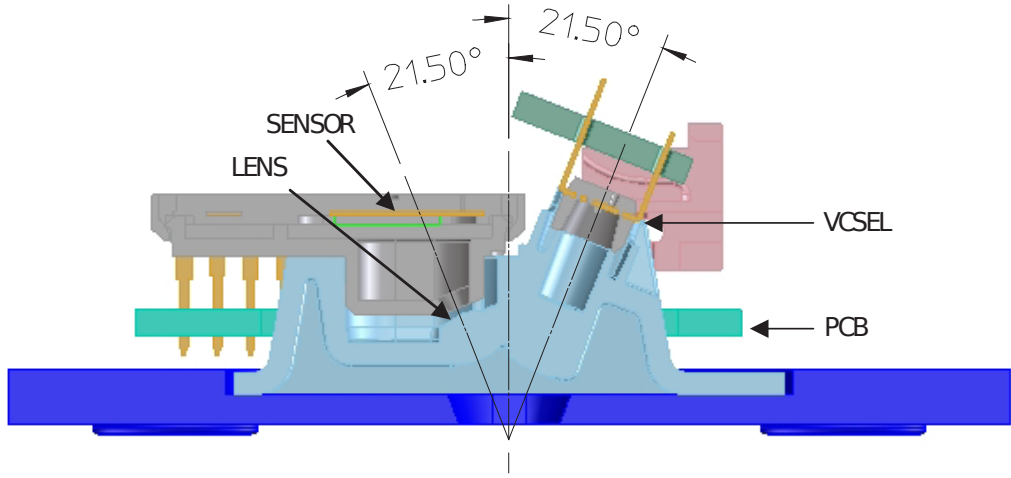


Figure 16: Original mouse set-up from the data sheet [2]. The optical rays from the VCSEL (right) and the sensor (left) meet on the surface.

With these informations we can estimate a focal length of 2.88 mm for the original mouse lens. With the distance of the sensor and object plane being the same of both sides of the lens, this leads to a magnification factor of 1. The measured aperture diameter (of the hole in the chip casing) on the original lens is 1.4 mm. The sensor delivers a quadratic image with a side length of approx. 0.92 mm. Therefore we get a maximum image size of 1.3 mm diameter.

These findings were confirmed by the simulation via WinLens. The WinLens sketch of the system can be seen in Figure 17. The according spot diagrams are satisfactory, see Figure 18. The simulation is done for $\lambda = 842$ nm, the wavelength of the illuminating VCSEL. The modelling of the first lens is used as base for the simulation of the extended optical systems in WinLens.

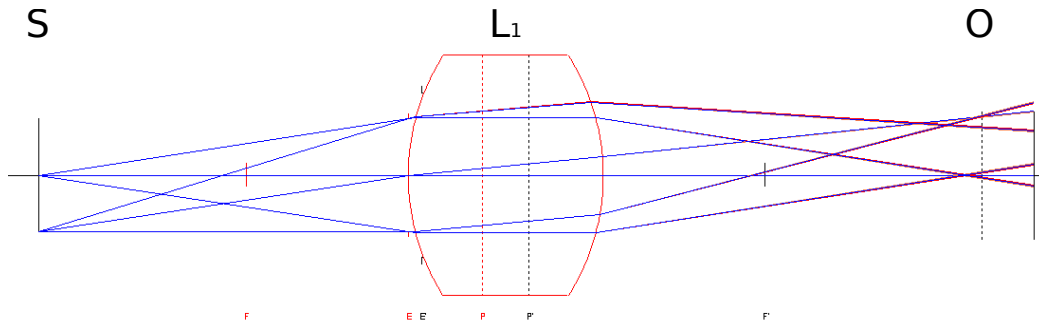


Figure 17: WinLens plot of the simulation of the unmodified optical system of the mouse. One single lens with $f = 2.88$ mm is exactly located in the middle between sensor plane S and object plane O.

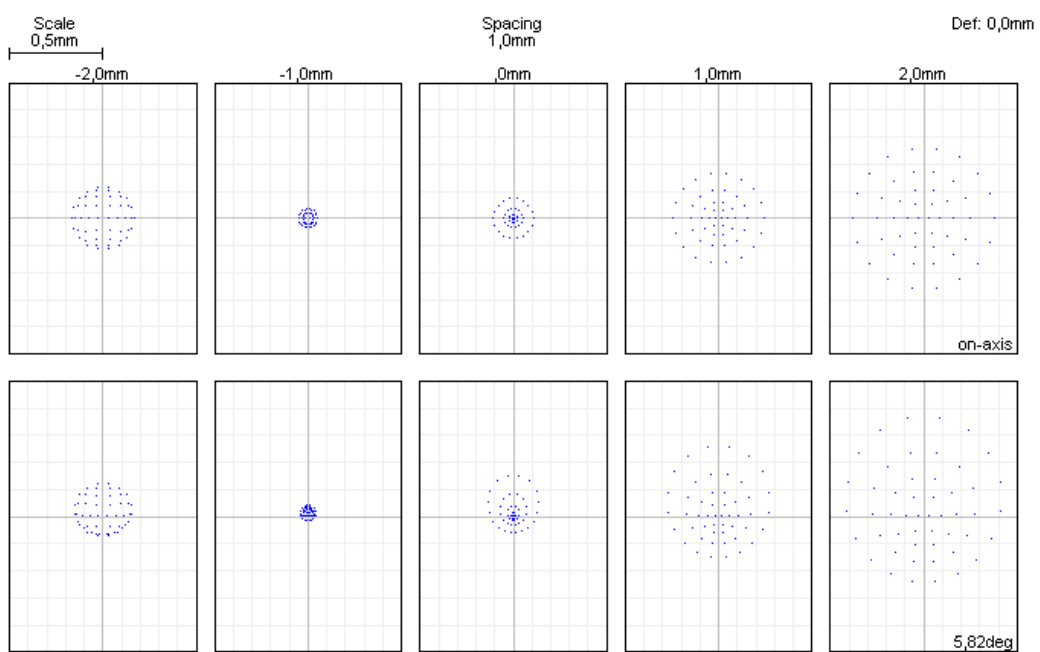


Figure 18: WinLens plot of the spot diagram of the simulation of the unmodified optical system of the mouse for $\lambda = 842 \text{ nm}$. The focusing of the spots hint to a relatively well modelled system.

4.2.2 Optical Path Calculations: 2-Lens Setup

The goal is to find a lens set-up that magnifies the current optical system by five times. We designed the system without telecentric at first, as a telecentric add-on does not alter the magnification of the system. For a magnifying system we added a second lens in front of the original system that has its image plane on the object plane of the original system (see Figure 19). The needed focal length f_2 of lens 2 is calculated from the Laplace projection equation [18]:

$$\frac{1}{f_2} = \frac{1}{o_2} + \frac{1}{i_2} \quad (1)$$

o_2 is the object distance, i_2 the image distance from the lens. We want to set $o_2 = 5 \cdot i_2$ for a magnification factor of five. From the range of possible values for o_2 , we are limited by the maximum available space for the odometry sensor in the robot. The extension of the optical system must be at most 80 mm long, therefore o_2 should be no longer than 65 mm.

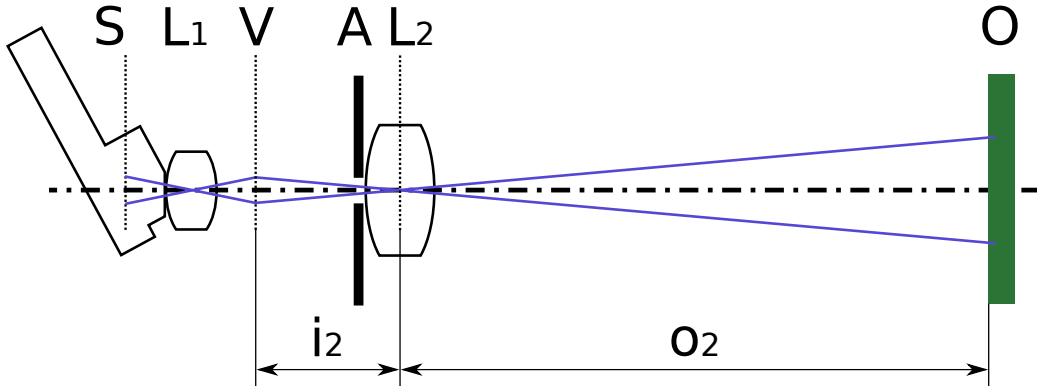


Figure 19: Sketch of the extension of the original system with a second lens. From left to right: Sensor plane S, original mouse lens L_1 , virtual image plane V (former object plane), second lens L_2 with new aperture A and new object plane O. Dimensioning below are: Image distance i_2 to virtual image and object distance o_2 for magnifying lens L_2 .

The next criteria for the lens system is the depth of focus. We wished ± 10 mm depth of focus to the object plane. For any symmetrical lens the depth of focus lies between the near and far limits, see Figure 20.

We therefore set the near limit $d_n = o_2 - 10$ mm and the far limit $d_f = o_2 + 10$ mm.

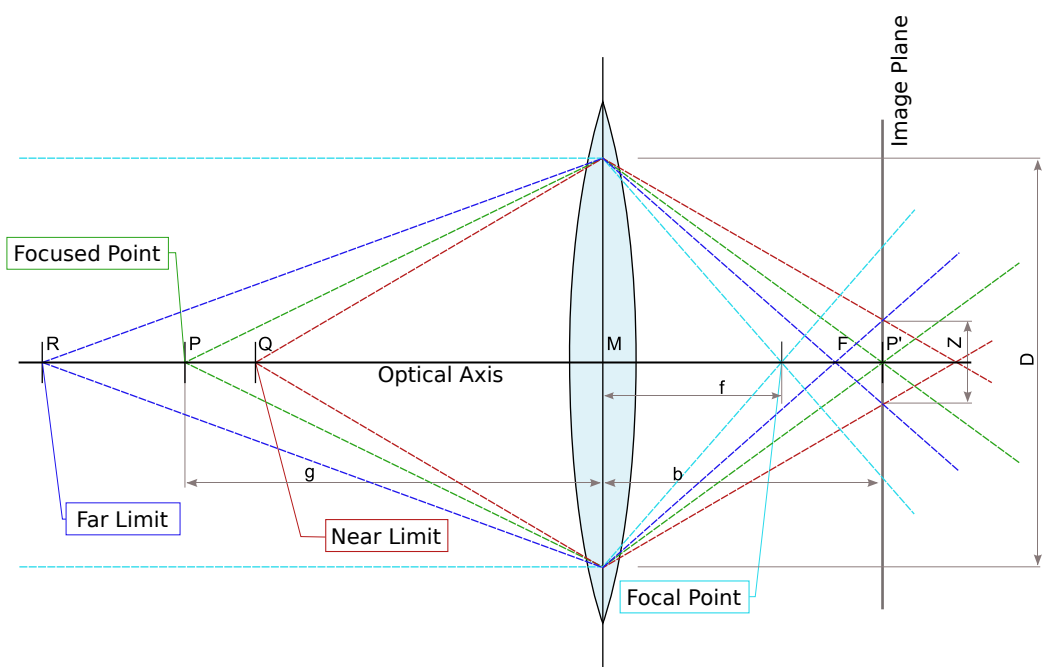


Figure 20: Definition of the depth of focus. The focused area lies between the near limit and the far limit. The limits are dependent on the focal length f , the aperture D , the image/object distance b/g and the allowed circle of confusion diameter Z .

Source: Wikimedia Commons¹, CC BY-SA 3.0.

¹ http://commons.wikimedia.org/wiki/File:Schaerfentiefe_hyperfokal_inkl_fernbereich.svg (last accessed 26.05.2011)

The formula for the distance of the near and far limit is the following:

$$d_{n/f} = \frac{g \cdot d_h}{d_h \pm (g - f)} \quad (2)$$

with $d_h = \frac{f^2}{\kappa \cdot Z}$ being the hyperfocal distance (3)

and $\kappa = \frac{f}{D}$ being the *f*-number. (4)

We see that the limits depend on the circle of confusion Z and the aperture diameter D . The circle of confusion can be easily calculated: our sensor is 0.92 mm wide and has a resolution of $30 \times 30 \text{ px}^2$. This leads to a pixel being $\approx 0.03 \text{ mm}$ wide. We use this value to estimate the maximum circle of confusion diameter $Z = 0.03 \text{ mm}$. We see that the only variable left responsible for the sharpness is the aperture diameter D . The calculations of the needed aperture diameter:
From Equation 1 and our magnification factor of five follows

$$f_2 = \frac{o_2}{6} \quad (5)$$

We use this to substitute κ (4) and f in d_h (3) to get a simplified formula for

$$d_h = \frac{o_2}{6} \cdot \left(\frac{D}{Z} + 1 \right) \quad (6)$$

This inserted into the formula for the near limit $d_n = o_2 - 10 \text{ mm}$ leads to the aperture diameter

$$o_2 - 10 = \frac{o_2 \cdot \frac{o_2}{6} \cdot \left(\frac{D}{Z} + 1 \right)}{\frac{o_2}{6} \cdot \left(\frac{D}{Z} + 1 \right) + o_2 - \frac{o_2}{6}} \Rightarrow D = Z \cdot \left(\frac{o_2}{2} - 6 \right) \quad (7)$$

The formula for the needed aperture diameter on the far limit is similar:

$$D = Z \cdot \left(\frac{o_2}{2} + 4 \right) \quad (8)$$

From these both formulas (7) and (8) we see that the needed aperture is linear dependent on the object distance and therefore from the length of the optical extension on a given magnification. Bigger apertures yield more light and with better illumination the sensor will achieve higher frame-rates due to a shorter shutter length. Therefore we want to maximize our aperture and we choose the longest possible object distance. From (5) and a maximum object distance of 65 mm we choose a lens with $f = 10 \text{ mm}$ on the upper limit, which leads to the following aperture diameters:

$$D_n = 0.672 \text{ mm}$$

$$D_f = 0.952 \text{ mm}$$

The real needed aperture is somewhere in the middle. Apertures in this range are possible to manufacture ourselves, which looks promising.

The next influence on the depth of focus is diffraction. Diffraction occurs when a wave encounters an obstacle. Due to the wave nature of light every spot of light results in an *Airy disc*, when passing a lens with a circular aperture. The best possible resolution of an optical system is the minimum distance, where two Airy discs can be distinguished. This distance is the radius of the Airy disc [18], see Equation 9.

$$\Delta x_{min} = r = 1.22 \frac{\lambda}{D} f \quad \begin{array}{l} f \dots \text{focal length} \\ D \dots \text{aperture diameter} \end{array} \quad (9)$$

The Airy disks must be at minimum one pixel ($30 \mu\text{m}$) apart to be distinguished. At $\lambda = 842 \text{ nm}$, with a focal length of 10 mm and an estimated aperture of 0.8 mm , the Airy disks are $12 \mu\text{m}$ apart according to Equation 9. This should be more than enough for these lens and aperture combination.

The system with a second lens with $f = 10 \text{ mm}$ is simulated in WinLens, see Figure 21. The according spot diagram can be seen in Figure 22.



Figure 21: WinLens plot of the simulation of the extended optical system with lens 2. From left to right: Sensor plane S, original mouse lens L_1 , aperture A, second lens L_2 and object plane O.

4.2.3 Optical Path Calculations: Telecentric Setup

Until now the magnification of the system (and therefore the measured speed) is linear dependent on the object distance, which we wished to vary about $\pm 10 \text{ mm}$. This would induce unacceptable errors from varying object distance. To counter that, the distance-dependent magnification can be eliminated by a telecentric attachment.

To make a finite conjugate system like ours telecentric, a lens with the focal length of the object distance has to be placed in front of the objective with its focal point set into the aperture of the objective [28]. The third lens is therefore placed at the position of the object of the 2-lens set-up, as seen in Figure 15 in subsection 4.2. As telecentric lens an achromatic doublet with $f = 50 \text{ mm}$ is used. This does

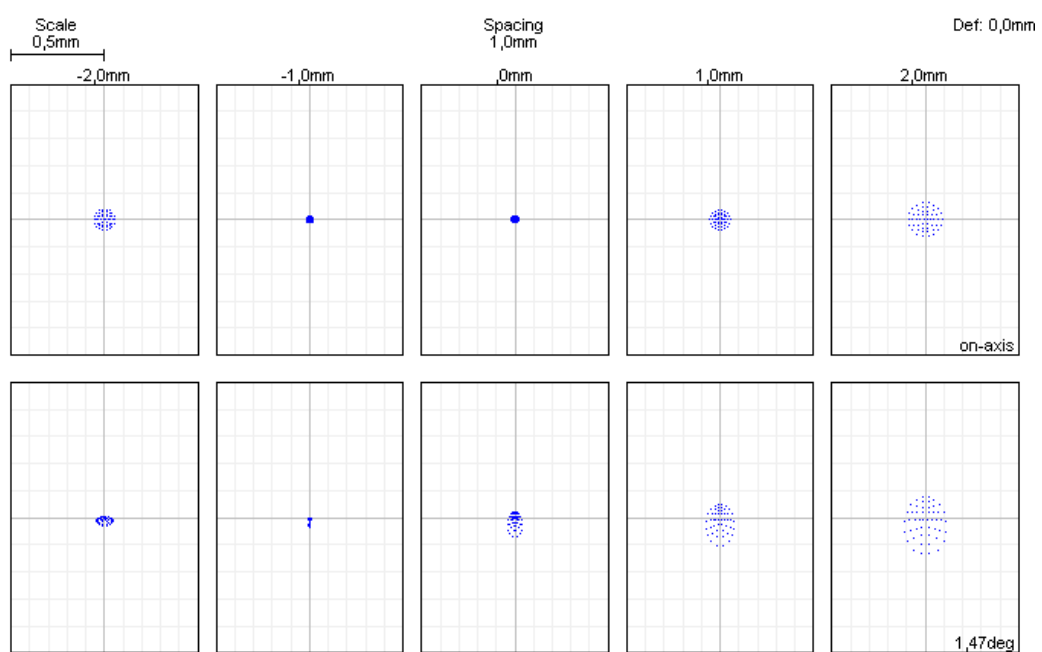


Figure 22: WinLens plot of the spot diagram of the simulation of the extended optical system with lens 2, $\lambda = 842\text{ nm}$. The focusing of the spots hint to a relatively well modelled system.

not alter the magnification and the sharpness remains in an acceptable range up to 30 mm from the telecentric lens. The choice of this lens type has been approved by WinLens simulation, see Figure 23 and Figure 24.

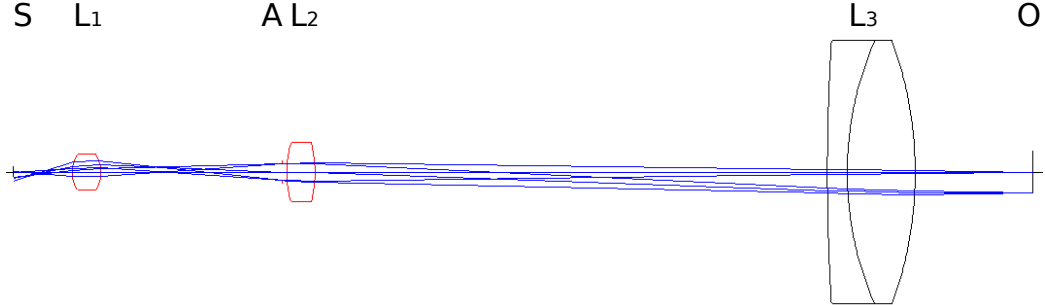


Figure 23: WinLens plot of the telecentric system with all three lenses. From left to right: Sensor plane S, original mouse lens L₁, aperture A, second lens L₂, third lens L₃ and object plane O.

4.2.4 Sensor Mounting and Calibration

The PCB for the ADNS-6010 (as shown in Figure 14 in subsubsection 4.1.4) is mounted on a Micro-Bench carrier. Its mount allows calibration of the sensor in x- and y-position as well as the angle of the sensor to the optical axis of the Micro-Bench. The PCB is mounted in an 21.5°-angle due to the angle of the optical axis on the ADNS-6010 (as shown in Figure 16). The mount and the position of all calibration screws is shown in Figure 25.

For calibrating the sensor to the optical axis of the Micro-Bench, it is mounted on the micro-bench with an 750 nm IR-laser that defined the optical axis. The set-up for calibration is shown in Figure 26. The 5 mW-laser has to be damped by a filter-array for the safety of the sensor. In front of the sensor is the magnification lens L₂, which allows for a more accurate calibration with its 5×-magnification factor. The sensor is connected to the microcontroller and the image of the sensor is read out and visualized on a computer screen (For details of this process see subsection 4.3). The sensor is calibrated to the optical axis by trying to move the laser speckle in the field of view to the centre by changing sensor position with the adjusting screws. A sample image of the laser pointing to the sensor from the sensor's view can be seen in Figure 27.

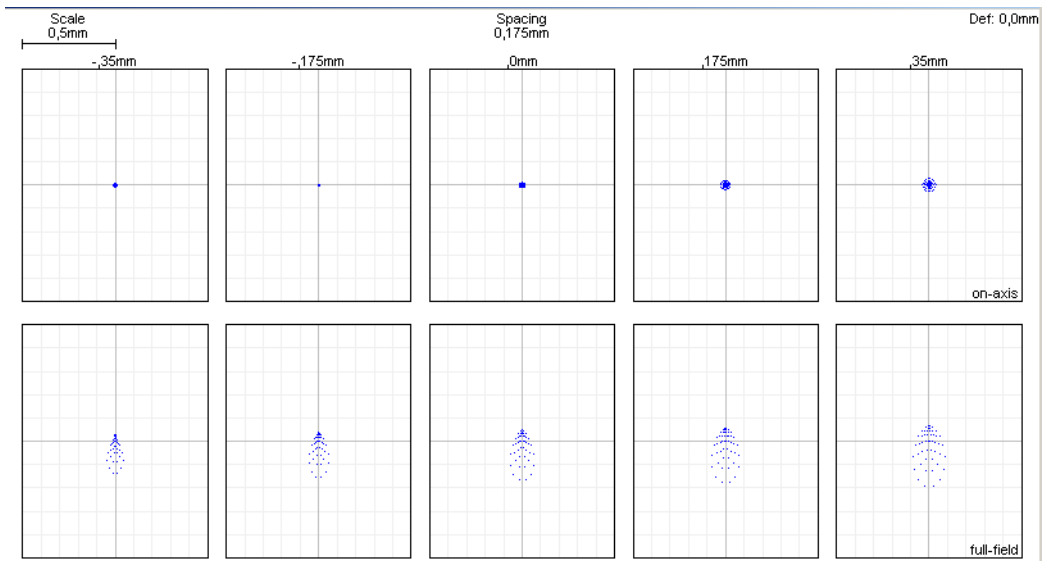


Figure 24: WinLens plot of the spot diagram of the simulation of the complete optical system, $\lambda = 842 \text{ nm}$. The focusing of the spots hint to a relatively well modelled system.

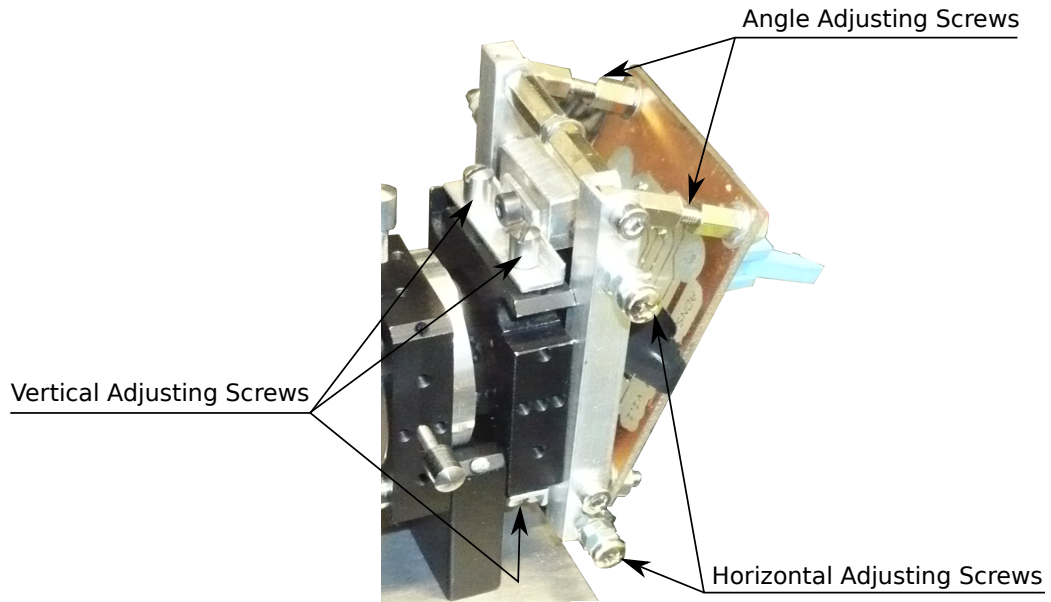


Figure 25: The PCB with the ADNS-6010 with its mount on a Micro-Bench carrier on the end of the Micro-Bench. It can be adjusted horizontal and vertical to the optical axis of the Micro-Bench. There are two pairs of opposite adjusting screws for each direction, horizontal and vertical. Its angle can be adjusted with the variable PCB-holding screws on top.

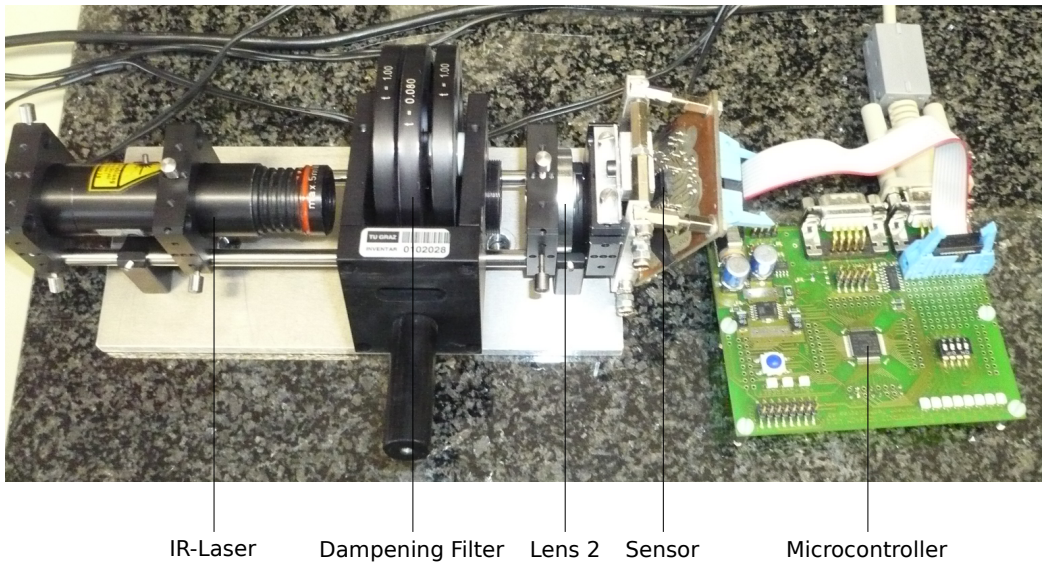


Figure 26: Set-up for calibrating the sensor to the optical axis of the Micro-Bench. From left to right: IR-laser, laser dampening filter, magnification lens 2 in front of the sensor and the microcontroller for reading out the sensor image.

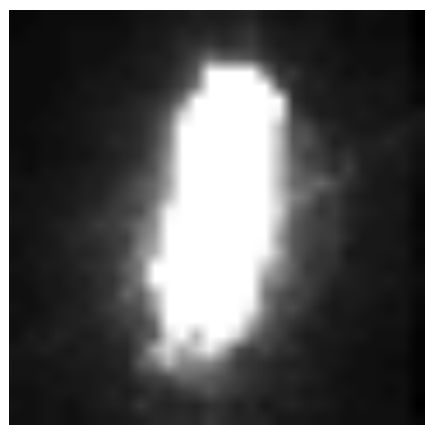


Figure 27: Image of the laser speckle in the calibration process from the sensor's view. $30 \times 30 \text{ px}^2$ resolution, $264 \mu\text{s}$ shutter length.

4.2.5 Lens 2 and Aperture Mounting

According to the calculations in subsubsection 4.2.2, a lens⁷ with $f = 10 \text{ mm}$ was ordered from Thorlabs⁸, along with an adapter⁹ to 12.7 mm ($1/2''$) diameter. Its small diameter (6 mm or 12.7 mm with adapter) is not compatible with any Micro-Bench carrier available. So a mount for both L₂ and the aperture is designed, which could be fixed in a 35 mm-Micro-Bench carrier.

The mount is turned out of aluminium with a cavity for the 12.7 mm lens adapter and mounting holes for the aperture. It has four M3 mounting holes, two for the lens holder and two for the aperture. The lens holder is held down by two bigger washers, the aperture mounted through its holes with distance washers. The complete assembly is shown in Figure 28. The UniGraphics drawing of the mount is available in the AFS¹⁰.



Figure 28: Lens mount for L₂ and the aperture. The lens in its adapter is held down by two washers, the aperture is mounted with distance washers as close as possible to the lens.

For the experiments a set of apertures with different diameters are made. They are made of copper-coated epoxy, normally used for PCBs. The apertures are a simple sheet of epoxy with the size $10 \times 40 \text{ mm}^2$, where the aperture is in the middle and two mounting holes matching for lens 2 mount outside. They are manufactured on the circuit board plotter of the Institute of Electrical Measurement and Measurement Signal Processing. The EAGLE files for the aperture plates are available in the AFS¹¹. Eight different aperture plates with aperture diameters 0.7, 0.8, 0.9, 1.0, 1.2, 1.5, 1.8 and 2.1 mm are manufactured. The apertures must be

⁷N-BK7 Bi-Convex Lens with IR-coating (LB1157-B)

⁸<http://www.thorlabs.de> (last accessed 08.01.2011)

⁹Adapter for $\varnothing 6 \text{ mm}$ Optics (LMRA-6)

¹⁰/afs/robocup.tugraz.at/mechanics/01_Krikkit3G/06_Odometriesensoren/CAD/Versuchsaufbau/Linsenhalterunghalterung/ (last accessed 08.01.2011)

¹¹/afs/robocup.tugraz.at/projects/2010_improved-odometry/platinen/Blenden (last accessed 08.01.2011)

mounted with the copper side facing the lens on the lens mount to be as close as possible to the lens surface.

4.2.6 Illumination

The original illumination for the laser mouse consists in a VCSEL laser diode with a wavelength of 842 nm. With the magnification system we have a much greater target area to illuminate for which the original VCSEL is too weak. The goal is to find a proper illumination for a target area of $5 \times 5 \text{ mm}^2$. It must be bright enough on every test surface (see subsection 3.1) to allow the automatic shutter control of the sensor to minimize the shutter for the maximum frame-rate. Other requirements are the available space on the robot for a sensor and the power consumption. The illumination must fit besides the optical ray path inside the space constraints of the $60 \times 60 \text{ mm}^2$ cross-section. The power supply is either 24 or 6 V and the cooling possibilities are limited by the space constraints.

The frequency of the illumination must be in the range of the responsivity of the ADNS-6010, see Figure 29. A monochromatic light source would be favoured as this would lead to higher contrast.

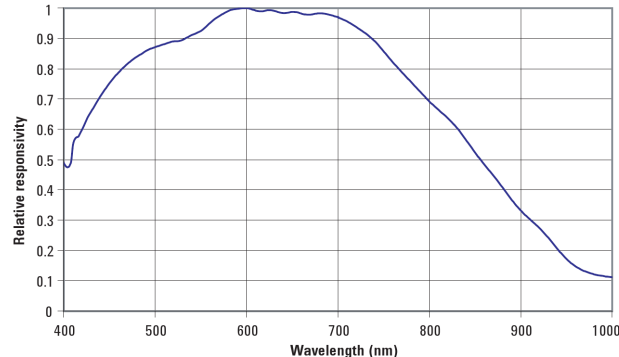


Figure 29: Relative responsivity for the ADNS-6010 laser mouse sensor from the data sheet [2].

Finding proper illumination is a difficult task as every tested surface reacts differently with each type of illumination. The illuminant tested are a 1 kW studio spotlight, the laser used for calibrating and different types of high-power LEDs. Every illuminant is tested on a white sheet of paper for reference and then on the three different carpets. For the experiments with the illumination it is required to achieve the maximum frame-rate of 7080 Hz (shutter below 18 μs) on all test surfaces accomplished by an acceptable surface quality (feature count around 100). The shutter/frame-rate and surface quality were read out via the PyQt-application

described in subsection 4.3.

The studio spotlight could not be focused enough on the $5 \times 5 \text{ mm}^2$ spot to achieve the needed luminous density needed to get the necessary frame-rate of the test surfaces. Example screen-shots of the studio spotlight illuminating the test surfaces can be seen in Figure 30 for every test surface. The studio spotlight would need more focusing optics to reach the needed luminous density and even using a smaller version would not fit on the robot. So smaller approaches follow next.

The laser used for calibration, due to its power and beam size being similar to the original VCSEL it was too weak to be used.

The best power/size rating can be achieved with LEDs. The brightest LEDs found were from LED1.de. Two types of LEDs were chosen for comparison, ultra-bright white LEDs and infra-red LEDs. Their specifications can be seen in Table 3.

Name	Nichia NSPW500GS-K1	Name	LED 5 mm infrared
Art. #	54400101	Art. #	50885002
Case	5 mm waterclear	Case	5 mm waterclear
Viewing Angle	15°	Viewing Angle	15°
Power	3.2 V	Power	1.5 V
Current	20 mA typ., 30 mA max.	Current	50 mA
Brightness	44 000 mcd	Intensity	120 mW
Price	9.99 € (10 pcs.)	Price	7.99 € (10 pcs.)
Chromaticity		Wave Length	850 nm (infrared)
Coordinates x/y	0.31/0.32		

Table 3: Technical data of both LED types evaluated. LEDs ordered from LED1.de, prices of 30.10.2010.

From each type of LEDs 20 pieces were ordered. Any single LED of these does still not provide enough luminous density, so an array of these LEDs is used. They must be mounted as close as possible to the target surface. The only possible mounting place on the micro-bench is between the second and the third lens, see Figure 31. They are mounted in a ring around the optical rays and illuminate the surface through the third lens. Therefore, a small PCB is designed¹² with nine LEDs in a circular array and an opening in the centre for the optical beam (Figure 32). It is designed to fit on the micro-bench and is then mounted on a micro-bench carrier.

From the PCB four pieces were manufactured for testing. They are populated with either white or infra-red LEDs. Power must be supplied by an external power

¹²EAGLE files are available in the AFS: /afs/robocup.tugraz.at/projects/2010_improved-odometry/platinen/LED_ring_v2 (last accessed 15.01.2011)

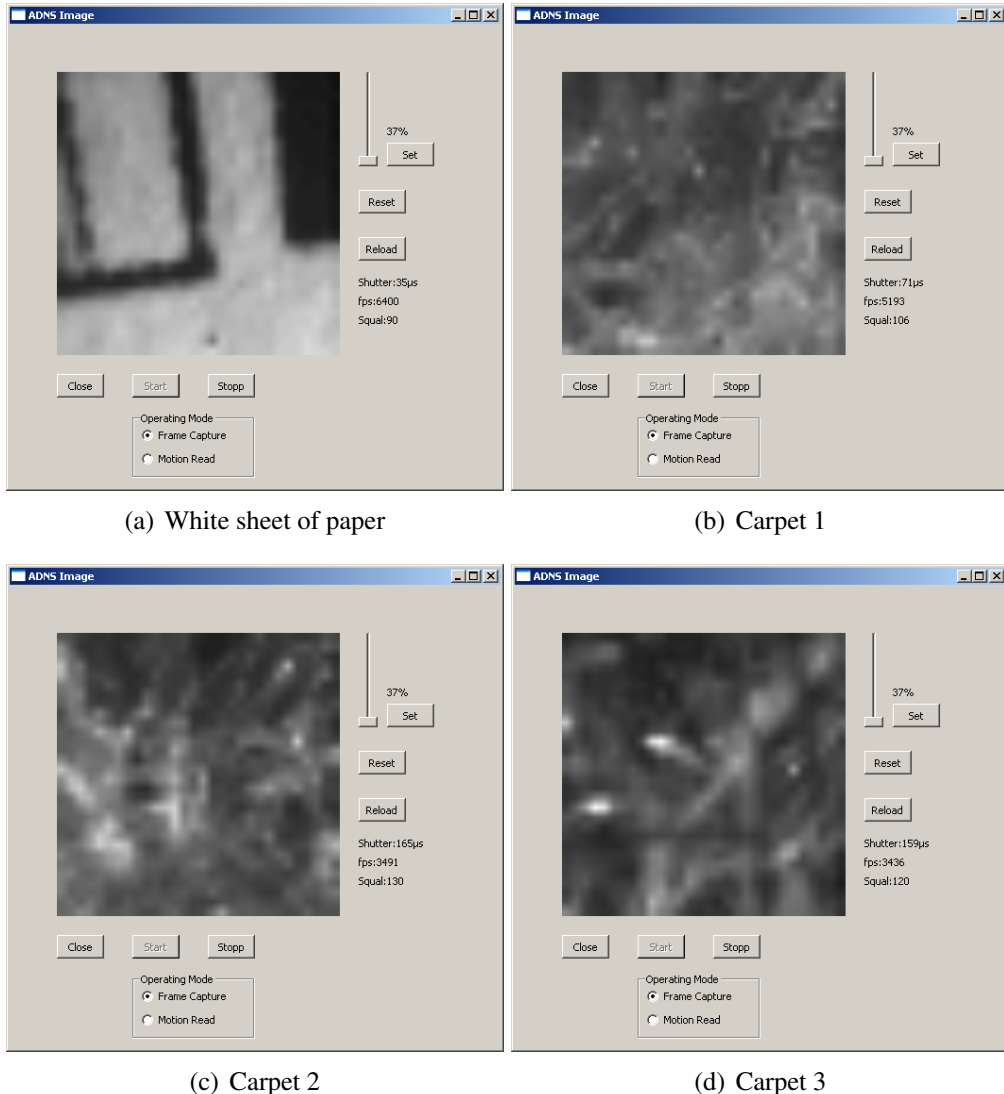


Figure 30: Screen shots of the four target surfaces (a–d) with illumination by the studio spotlight. The distance of the spotlight to the surface was 17 cm. An aperture of 1.0 mm was used. The surface quality (Squal) of all samples is sufficient, but the needed frame-rate (fps) of 7080 Hz is not reached anywhere. The software used is described in subsection 4.3.

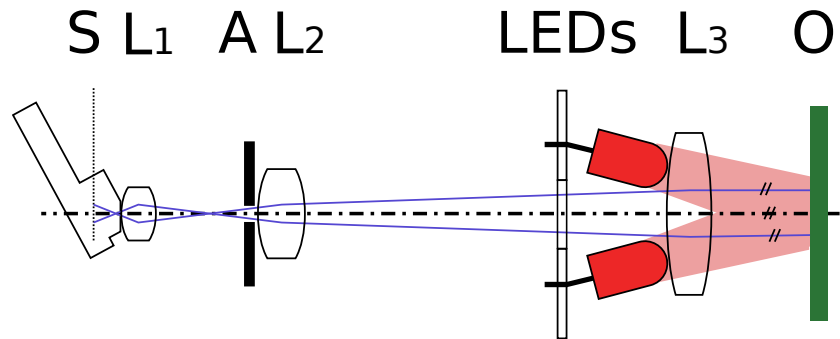


Figure 31: Complete optical system with illumination. The LEDs are placed on a PCB in a circle around the optical ray path and illuminate the object surface (O) through the third lens L_3 . The effect of the third lens on the illumination rays is negligible.

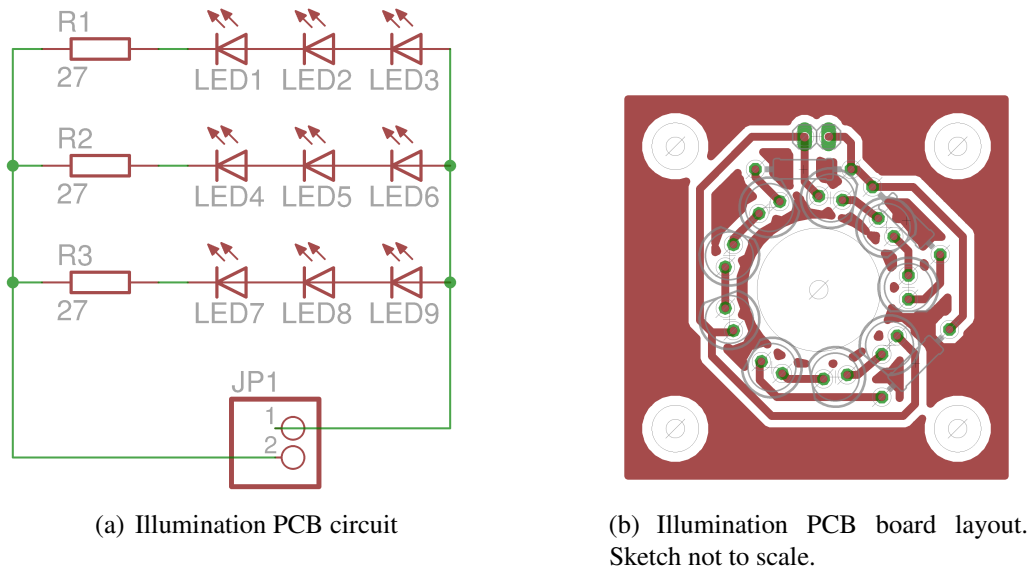


Figure 32: Illumination PCB circuit and layout. The PCB is designed to be mounted on the micro-bench with the corner-holes and measures $40 \times 40 \text{ mm}^2$. Nine LEDs are arranged around the centre hole for the optical rays. To reduce the needed overall voltage, they are arranged in three parallel lines with three LEDs and a series resistor each. The power supply is to be connected on a simple 2-pin header on top.

supply unit. Both LED types are to be powered with a constant current source. According to Table 3, for the PCBs with white LEDs for which a maximum current of 30 mA is allowed, 90 mA for the three lines are used and 150 mA for the infra-red LEDs. With the serial resistor it leads to a needed voltage of \approx 22 V for the white LEDs and \approx 10 V for the infra-red LEDs. It would be possible to achieve more luminosity with the LEDs operating at higher currents in PWM mode (using the PWM signal for the original VCSEL from the sensor), however the constant current luminosity was enough for the experiments.

The nine LEDs need to be aligned to point exactly to the target centre for the maximum effect. Every LED on the PCB is calibrated separately to point to the centre. For the white LEDs this can be seen in Figure 33. The infra-red LEDs are calibrated via the streamed video from the sensor, as their light (850 nm) is invisible for the human eye.

A note on the cooling of the LEDs: They got very warm, but this was no problem in the open testbed. When tightly packed inside the robot an appropriate cooling strategy must be considered.

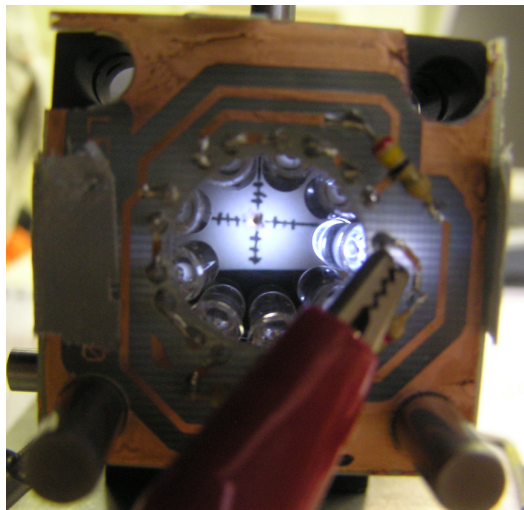


Figure 33: Calibration of the LEDs to point to the centre for maximum effect. The angle of every LED on the PCB is calibrated separately to point to the marked centre.

When comparing the white and infra-red LEDs, the infra-red LEDs perform slightly better, so the experiments are done with infra-red illumination.

4.3 Software

The software required for controlling the sensor is split into two parts: The low-level interface for directly communicating with the ADNS-6010 laser mouse sensor is implemented in the microcontroller software written in C. The software on the microcontroller is again commanded from the user interface running on the PC written in Python and Qt (PyQt).

The user interface displays the images read from the sensor or logs motion data into text files. These text files are analysed and the results are plotted with octave.

4.3.1 Microcontroller-Software

The microcontroller software is written in C and developed with the Keil¹³ IDE. The Keil IDE produces hex files (*.H86), which are flashed over the serial port (RS-232) to the microcontroller development board. For the flashing process, see the board manual [17]. It is important to use a high quality serial cable to avoid bit-errors during the flashing process. The full source code of the software and the hex-binary is available in a git repository¹⁴.

The software on the microcontroller should fulfil the following functions: Catch the firmware in stage 1 and in stage 2 flash the ADNS-6010 with the new firmware, read out images and motion data.

The microcontroller is connected to the PC via RS-232. For communication via a terminal emulator from the PC an interactive console has been implemented based on the motion controller code [21].

For the firmware catch the synchronous serial interface (SSC0) in slave mode is used together with an analogue input, where it waits for the reset signal from the original microcontroller. The firmware is stored in the internal RAM of the microcontroller and can be output after the catch in human readable form on the terminal. Due to the available RAM in the XC164-CM, being smaller than the firmware size, the catch has to be split up. It must be repeated with an offset given for four times until the complete 1936 Byte of the firmware are available. After the firmware is known it is integrated into the microcontroller program as static array and can be flashed to the ADNS-6010 any time at stage 2. The listening of the communication between the original mouse microcontroller and the ADNS-6010 revealed other interesting data: After the firmware is flashed the self test on

¹³Keil uVision3 V3.30a © Keil Software Inc. downloadable from: <http://www.keil.com> (last accessed 25.05.2011)

¹⁴git://marvin.robocup.tugraz.at/git/uc_impresso_testbed.git (last accessed 15.01.2011)

the ADNS-6010 is triggered and the CRC of the firmware is checked. Then some configuration parameters are set for the ADNS-6010: The strength of the laser diode is set to 80 % and the laser shutter mode is disabled. At last the resolution is set to 800 dpi before starting motion read.

For the read image of the sensor the image can either be output as PGM image on the terminal or as binary data for use by the GUI. It is interesting that the firmware must not be loaded on the ADNS-6010 before an image can be read out. This largely increases the possible frame-rate of the video. The bottleneck in video streaming is the serial line from the microcontroller to the host computer. Therefore the speed of the RS-232 interface is increased to 115.6 kbit/s, more is not possible with Windows XP. With an image size of 900 Byte, a maximum frame-rate of 5 frames per second can be achieved, which makes the optical calibration processes very comfortable.

In motion read mode the read motion values from the ADNS-6010 are continuously output on the serial port. Before motion read the firmware must be loaded to the ADNS-6010. Data from the reference speed sensor (see subsection 5.2) is acquired in an interrupt-driven background thread and the current reference speed is output in addition to mouse sensor speed for comparison.

4.3.2 PyQt GUI

The microcontroller can be controlled completely via a command-line interface from a terminal emulator on the serial line. For displaying live images from the sensor a graphical user interface (GUI) is needed. Therefore a small GUI is developed, which can display images from the sensor and save motion data in a more convenient way. The GUI is written in the Python¹⁵ scripting language with a Qt¹⁶ graphical user interface (PyQt¹⁷). The PyQt environment is chosen because of its cross-platform ability and the simple ways of creating a GUI. The complete program with installation instructions is available in a git repository¹⁸. On Python modules *PyQt4* and *serial* are needed. The program uses the first serial interface (ttyS0 on Unix or COM1 on Windows), this can be changed in the constructor of the *OdoFrame*-class. The program is written completely threaded and has two operation modes: Frame Capture and Motion Read.

The common controls and indicators for both modes are explained in Figure 34. It is possible to set the laser strength, load the firmware or reset the ADNS-6010

¹⁵<http://www.python.org/> (last accessed 17.01.2011)

¹⁶<http://qt.nokia.com/> (last accessed 17.01.2011)

¹⁷<http://www.riverbankcomputing.co.uk/software/pyqt/intro> (last accessed 17.01.2011)

¹⁸git://marvin.robocup.tugraz.at/git/impodo_gui.git (last accessed 17.01.2011)

independent from operating mode. After reset the firmware must be loaded again if needed.

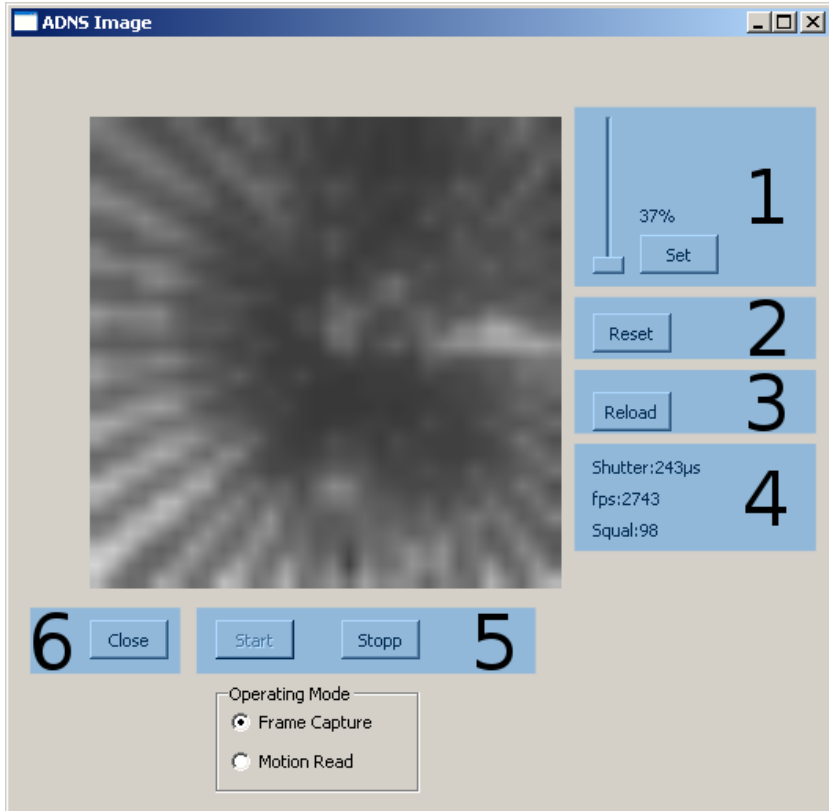


Figure 34: Screen-shot of the GUI with common controls and indicators. On the right side controls with direct reference to the ADNS-6010: Setting for the integrated laser driver with a range slider, where laser strength can be chosen between 37% and 100%. The setting is applied with the “Set”-Button (1). The reset line for the ADNS-6010 is toggled with the “Reset”-Button (2). The firmware of the ADNS-6010 can be reloaded with the “Reload”-Button (3). Indicators for current Shutter, frame-rate (fps) and surface quality (Squal) in count of features (4). Beginning of frame capture or motion read is controlled with Start/Stop - Buttons (5). The “Close”-Button terminates the program (6).

In frame capture mode live images from the ADNS-6010 are displayed as a video with 5 frames per second. After pressing the “Start”-Button a frame is captured and after the ADNS-6010 is reset the next frame is read. This continues in a loop until the “Stop”-Button is triggered. It is not necessary to load the firmware before the frame capture, but it will be loaded before every frame if it was loaded from the beginning. The display of the current shutter, frame-rate and surface quality is

updated with each image.

In motion read mode the display changes to a tabular view, where the current and accumulated motion data are displayed. This view and the description of the entries is shown in Figure 35. The firmware must be loaded before motion read can be started. After pressing the “Start”-Button the motion read from the ADNS-6010 is started. Additionally to being displayed all received data are written to a log-file. Data are written in comma-separated value format, which is intended to be used as input for the octave analysis scripts described subsequently.

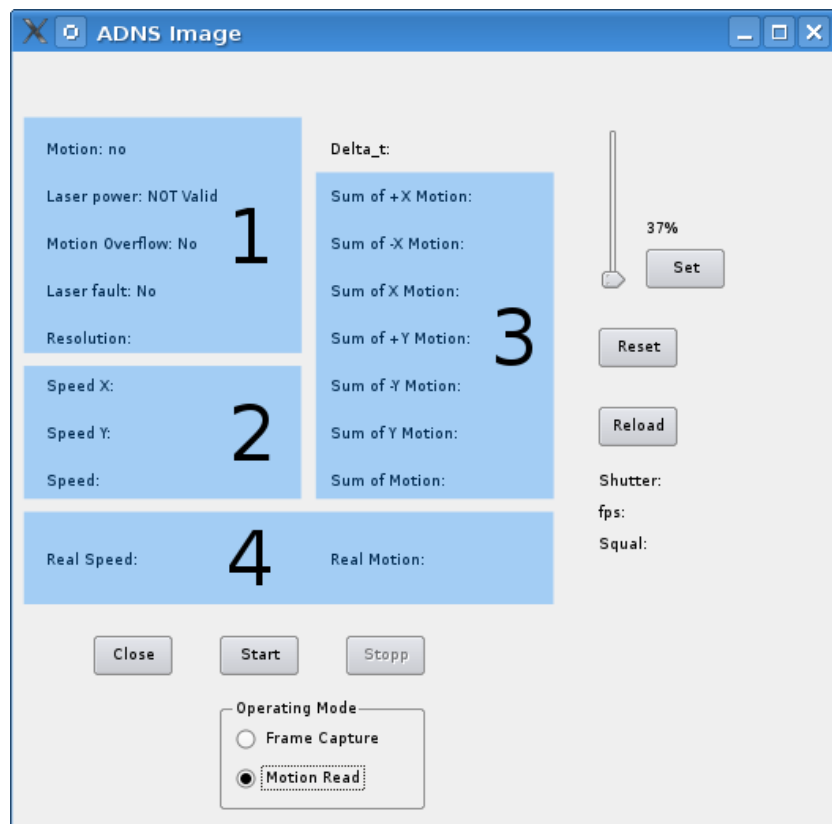


Figure 35: Screen-shot of the GUI in motion read mode. Section 1 displays some status details of the ADNS-6010. Section 2 shows the current speed calculated from the motion readings. Section 3 shows the distance covered from the beginning of the motion read by accumulating every dimension. Section 4 shows the speed and accumulated distance from the reference sensor connected to the microcontroller.

4.3.3 Octave Analysis Scripts

Mathematical data analysis is done in the GNU Octave¹⁹ language, similar to Matlab. The scripts process the csv-files produced with the GUI in motion-read mode. They are available in the same git-repository²⁰ as the GUI. The scripts are used for two purposes: Plotting motion data compared with the reference speed sensor, and providing a statistical analysis of the error-rate resulting from the comparison with the reference sensor. All results found in section 6 are produced with these scripts.

For plotting motion data is split into 100 ms-blocks. Motion data and data from the reference speed sensor is then plotted over time via gnuplot²¹. Motion data delivered from the ADNS-6010 are not related to any dimensional system, they are simply counts of pixels of how far the sensor has traversed. The scripts calculate a conversion factor to the metrical system by comparing the values with the reference sensor. The error rate calculated with the scripts equates to the deviance from the mean conversion factor for each test series with different speed.

¹⁹<http://www.gnu.org/software/octave/> (last accessed 20.01.2011)

²⁰git://marvin.robocup.tugraz.at/git/impodo_gui.git (last accessed 24.05.2011)

²¹<http://www.gnuplot.info> (last accessed 20.01.2011)

5 Experimental Set-Up

The goal of the experiments is to test the sensor on the required surfaces with speeds up to 5 m/s at varying distances. Therefore a testbed has to be build which allows the sensor to be tested on moving surfaces. To simulate a moving surface it was chosen to use a rotating disk on which different carpets can be mounted. The sensor with its complete optical system and illumination should point to the moving surface and measure their velocity at varying distances to the surface. Additionally, the rotational speed of the disk should be measured with a reference sensor. The block diagram of the whole testbed is shown in Figure 36.

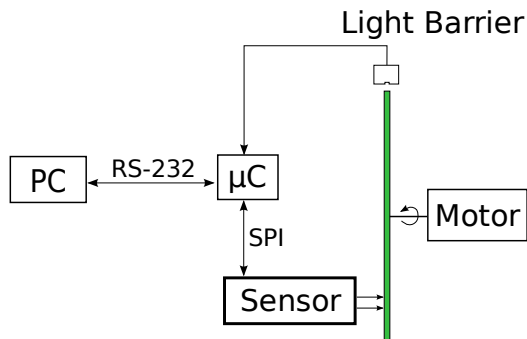


Figure 36: Block diagram of experimental setup: a rotating disc covered with different types of carpet simulates the game field. A light barrier sensor is used as a reference for the mouse sensor results.

The testbed consists of the mounting of the disk and its motor, the sensor with illumination, the microcontroller controlling the mouse sensor and the reference sensor, the host PC and the power supply for all components. The disk with its motor are mounted on a frame with alumina profiles, with the mouse sensor, microcontroller and reference sensor attached. The components were assembled in the laboratory of the Institute of Electrical Measurement and Measurement Signal Processing, as shown in Figure 37.

5.1 Motor and Disk

A motor from a hand drill is used to drive the disk. It runs on direct current and needs a stronger power supply which is able to supply 5 A at 12 V. We used a EA-PS 2016-100 laboratory power supply for the motor. The motor has a very uneven angular velocity, this can be seen in the plots over time in section 6.

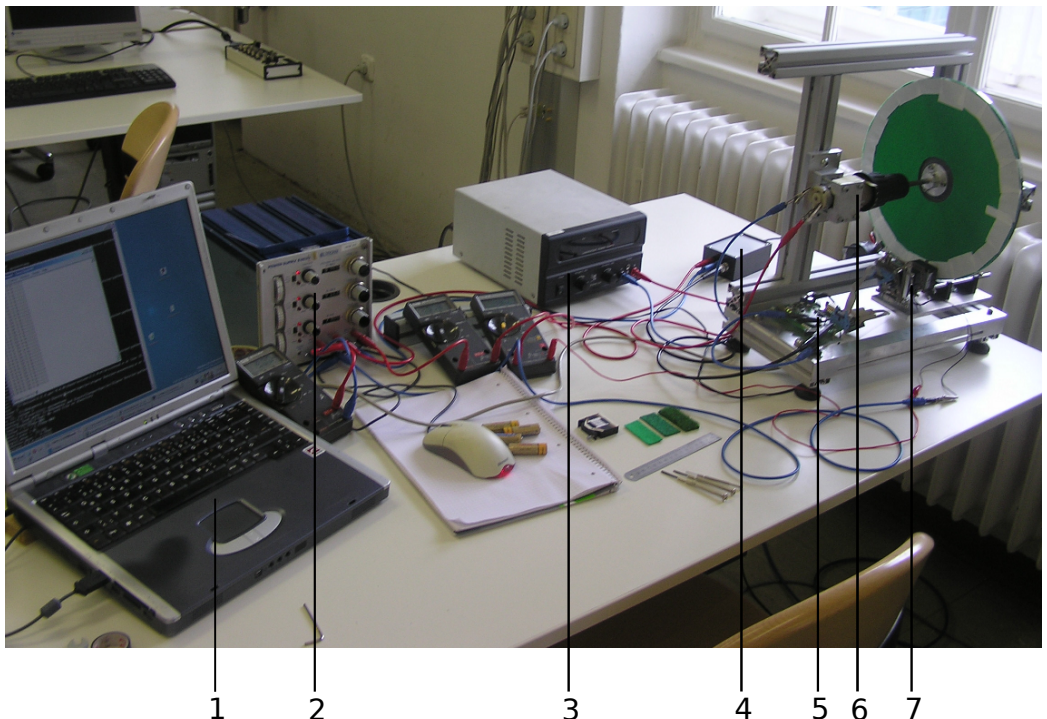


Figure 37: Photo of the experimental set-up in the laboratory: (1) Host PC running the user interface. (2) Power supply for the illumination and the reference sensor. (3) Power supply for the motor. (4) Reference sensor link box. (5) Micro-controller board. (6) Disk motor. (7) Sensor with optics and illumination.

The disk is made of plastics material with a thickness of 5 mm. It has a diameter of 295 mm and therefore a circumference of 927 mm. It is mounted on an axle with a bearing on the back side and is clamped into the drill chuck on the front side. It was manufactured at the Institute of Production Engineering²². The three different carpets (see subsection 3.1) are mounted with twin-sided adhesive tape.

5.2 Reference Speed Sensor

As reference speed sensor a light barrier is used to measure the rotation speed of the disk. A *HOA1404 Reflective Sensor* [14] from *Honeywell* is used. On the disk edge eight reflective elements made of alumina foil with a length of 28 mm are glued in even intervals. The light barrier is mounted 5 mm away from the disk edge (see Figure 38).

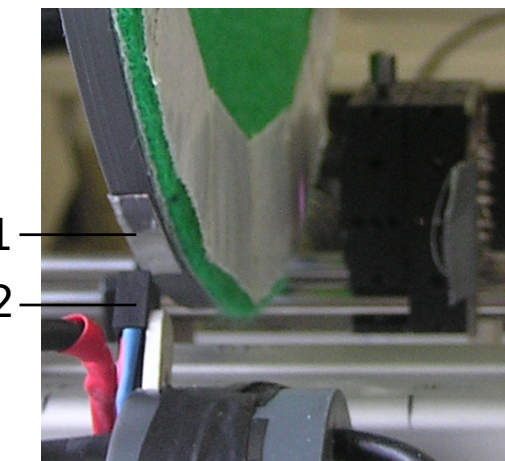


Figure 38: The reference speed sensor. A reflective sensor (2) points to the edge of the rotating disk, where the reflective elements (1) pass in front of it.

The reflective sensor consists of an infra-red LED and a photo transistor. Whenever a reflective part on the rotating disk passes below the sensor, the output voltage of the photo transistor changes.

The sensor came with a link box where its circuit is contained. The link box has connectors for power supply and sensor output. The IR-diode is specified with a current of 30 mA [14]. When taking the circuit in the box into account ≈ 22 V must be applied to the power supply connector. The output on the box is connected to an ADC on the microcontroller. On the microcontroller board a voltage

²²<http://www.ift.tugraz.at> (last accessed 11.02.2011). Thanks to Mr. Ingo Riemen-schneider.

divider is set up to convert the 22 V sensor output to the 5 V input range of the ADC. The complete circuit is shown in Figure 39. On the microcontroller the ADC of port 5.6 is used. The ADC is set to run with a frequency of ≈ 20.8 KHz. The detection of changes of the reflective state is outfitted with a small hysteresis function to prevent single errors. The speed is calculated from the time between two passes of reflective elements in front of the sensor.

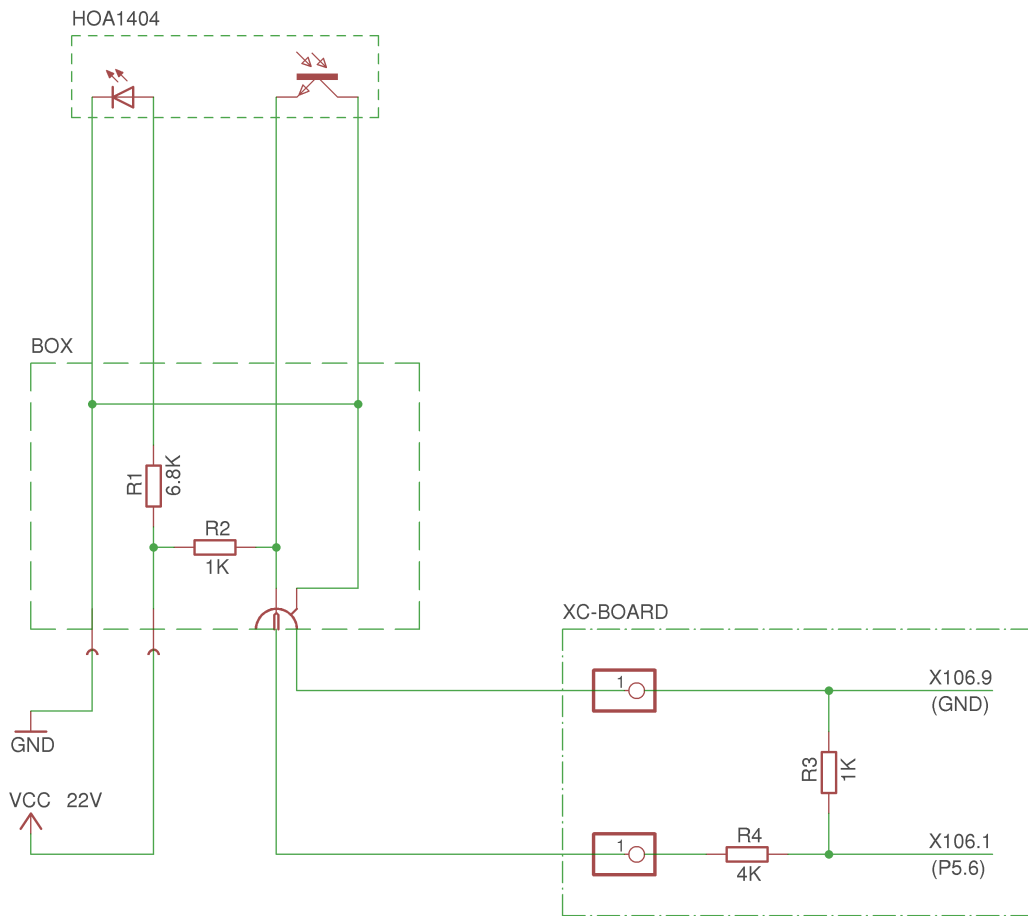


Figure 39: Circuit of the light barrier. On top is the HOA1404-sensor with the illuminating IR-LED and the photo transistor. It is connected via a 4-wire cable with the link box (middle). The link box is to be supplied with 22 V DC. The output on the link box is implemented as BNC plug. It is connected to the XC devel-board where a voltage divider is soldered before the ADC on port 5.6.

5.3 Microcontroller and Host PC

For the microcontroller development board 12 V DC power supply with a coaxial power connector is needed. An old wall power supply is used therefore. The microcontroller is connected to the sensor via a 10-pin cable to the sensor and via a serial cable to the host PC.

The host PC must be equipped with a serial port (RS-232) able to run the following software:

- Infineon MemTool for flashing the software to the microcontroller
- A terminal emulator (e.g. Tera Term²³) connected to the serial port at 115.6 kbit/s
- Python and QT for the GUI described in subsubsection 4.3.2
- Octave and gnuplot for the analysis scripts described in subsubsection 4.3.3

For the experiments a laptop, running Windows XP, is used.

²³Tera Term v4.62 used. <http://ttssh2.sourceforge.jp/index.html.en> (last accessed 25.05.2011)

6 Experimental Results

In all of the experiments the correlation of our sensor with the reference sensor is evaluated. The sensor is tested under the following conditions:

- Telecentric/non-telecentric set-up
- Different distances to the surface
- Different surface types (carpets/game field lines)
- Different orientations of the sensor

Every type of experiment was done in different speeds ranging from 1 – 5 m/s in steps of one. In the experiments sensor data were output with the PyQt GUI and recorded as csv-file. The typical procedure of an experiment:

- Visual control of the sharpness and frame-rate with the frame-capture mode of the GUI.
- Spinning up the motor to the desired speed. Speed display via the *testADC*-function on the CLI of the microcontroller with the terminal emulator.
- In the GUI: load the firmware and in motion read mode, *Start*, wait at least five seconds to accumulate enough data and *Stop*.
- Load the written .csv-file into octave and control the plot.

A typical experiment plot series is shown in Figure 42.

The .csv-files for all experiments are available in the AFS²⁴.

6.1 Non-telecentric Tests

At the beginning tests without the telecentric lens were made. The experiments showed a nearly linear dependence of the measured speed from the surface distance. This can be seen in Figure 40. When comparing results at a distance between 50 mm and 65 mm, there was a difference of up to 30 % in the measured speed, due to the varying magnification. Therefore a non-telecentric system is not eligible for our application.

The according standard deviations and bias for each series can be seen in Figure 41.

²⁴/afs/robocup.tugraz.at/projects/2010_improved-odometry/versuche/logs.tbz (last accessed 26.05.2011)

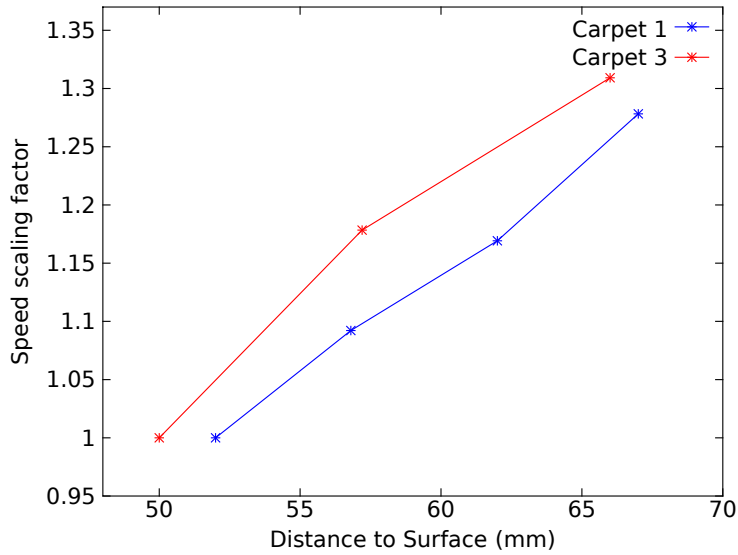


Figure 40: Speed deviation for non-telecentric system for varying clearance heights. The non-telecentric system induces a linear error dependent on the surface distance. With deviations of 30 % on our needed working range, the non-telecentric system is clearly not eligible for our application.

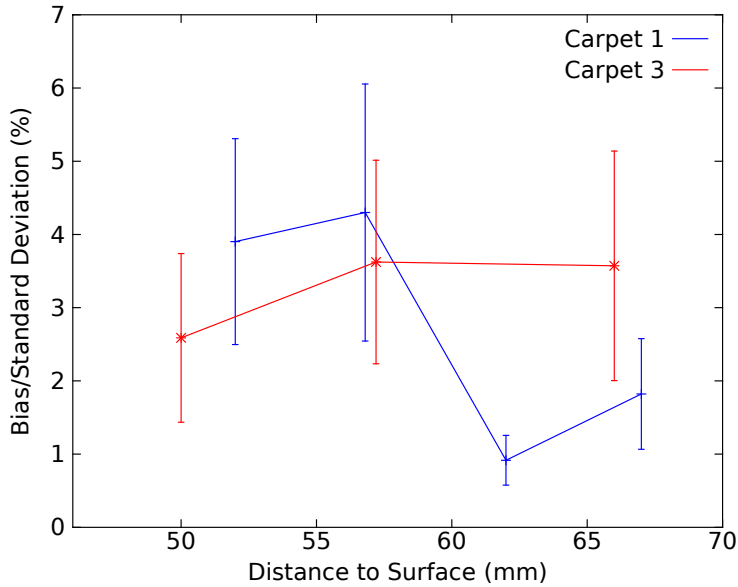


Figure 41: Bias and standard deviation for non-telecentric tests. With deviations below 5 % within each fixed distance the results would be acceptable for constant surface distance.

6.2 Telecentric Tests

For every carpet a number of tests with varying distance was done. The distances tested depend on the hair length and unevenness of each sample. A typical series of tests is shown in Figure 42. Notable is the wave form of the measured speed which corresponds with the uneven angular velocity of the motor. The amplitude decreases on higher speeds, because the moment of inertia has a greater effect on higher rotation speeds.

6.2.1 Carpet 1

Carpet 1 has a very even surface, which allowed the greatest height variations. Test series were made with the following distances: 3-5 mm, 5-8 mm, 10-13 mm, 13-16 mm and 16-19 mm. The plastic disk itself was warped due to manufacturing and the resulting level difference is about 3 mm, which is reflected on the given clearance height ranges.

Shown in Figure 43 are the results from the test series of carpet 1 for the five distance ranges.

A second series of tests was done with different orientations of the sensor. On a fixed distance the sensor was rotated in four 90°-steps. The results for each series for each rotation step are shown in Figure 44. The sensor shows a tendency to favour some directions. With steady deviations around 3 % for each direction it is advised to implement a software correction system depending on the current direction of movement.

6.2.2 Carpet 2

Carpet 2 was tested in the following ranges: 4-7 mm, 7-10 mm and 9-12 mm. The results are shown in Figure 45.

6.2.3 Carpet 3

Carpet 3 is the thickest sample with greater deviations in hair length, so only two series with different ranges were made, 3-6 mm and 5-8 mm. The results are shown in Figure 46.

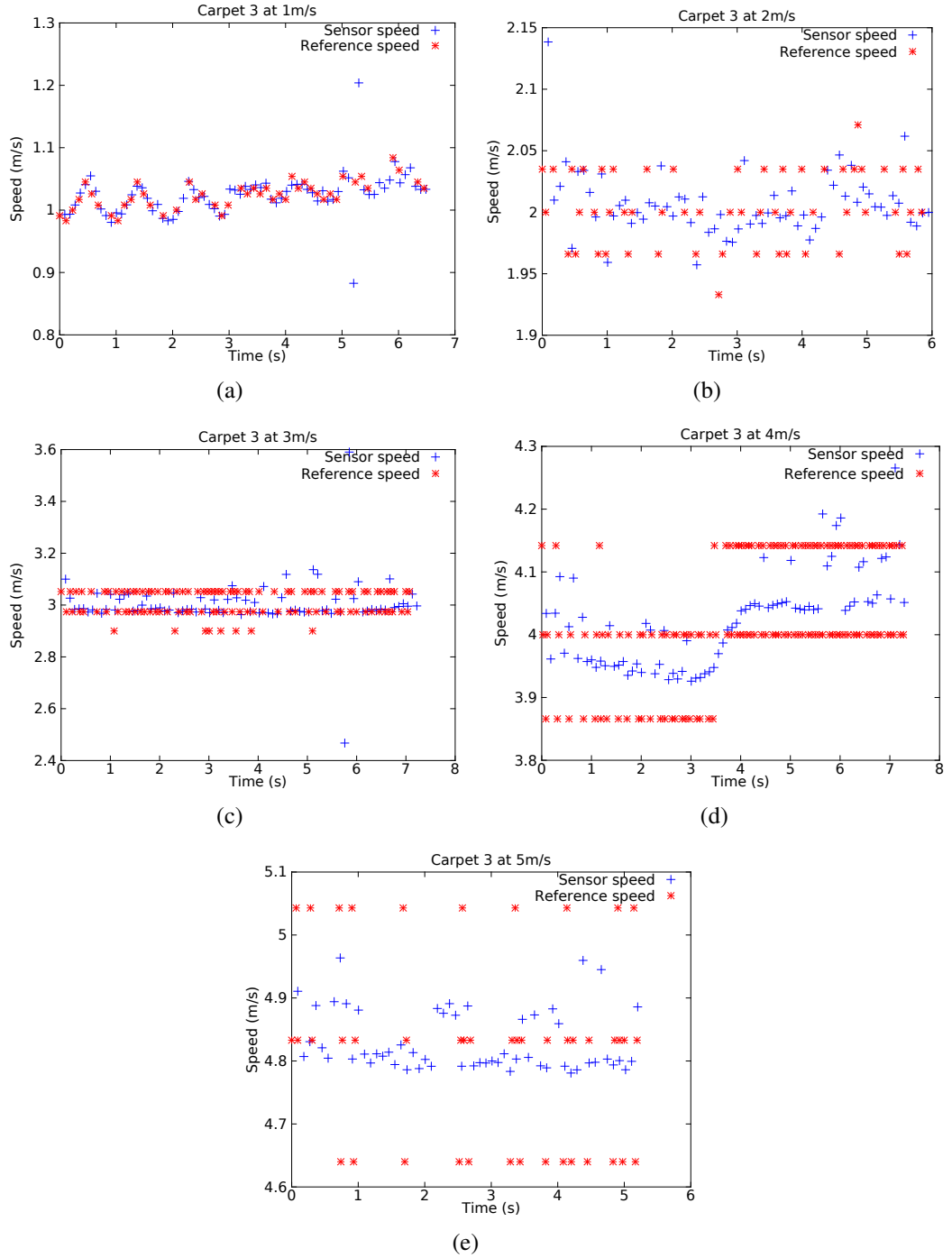


Figure 42: A typical test series with five different speeds. For example the series with carpet 3 at a distance of 3-6 mm is shown. Notable is the much less accuracy of the reference sensor compared to our sensor. This is of minor importance because the sensor is calibrated to the median of the reference sensor over a few seconds.

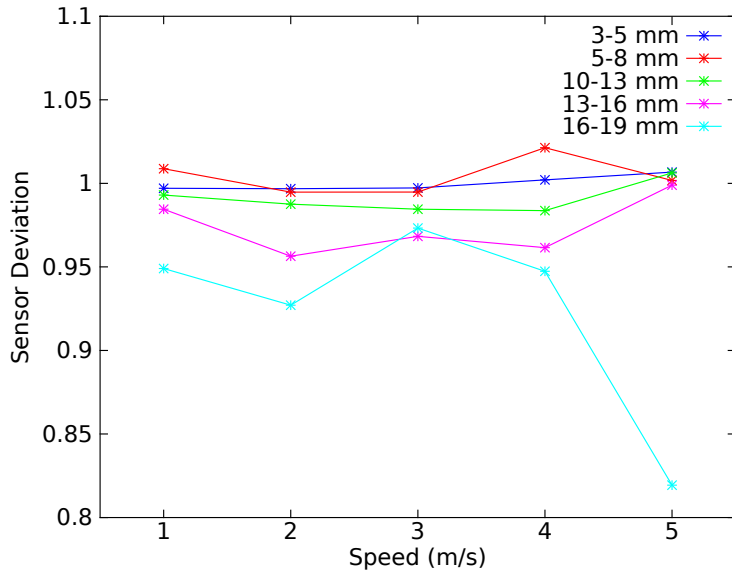


Figure 43: Results for carpet 1 and five distance ranges. Shown are the calibration factors of every single experiment compared to the mean value of 1 m/s. A slight tendency of the sensor to display lower than real values at higher speeds can be observed. The outlier on 16-19 mm at top speed is likely related to insufficient illumination.

6.2.4 Game Field Lines

The game field lines of a RoboCup game field consist normally in white gaffer tape on top of the carpet. It has the downside of being highly reflective and featuring very little contrast. With the illumination of white or IR LEDs, it leads to a surface feature count which is not high enough for tracking. With the different surface feature count we are able to distinguish white lines from the green carpet. This information is vital for our sensor fusion system to ignore our sensor data while moving over white lines and meanwhile extrapolate the motion. The features used for distinguishing between lines and “better” surfaces are shown in Table 4.

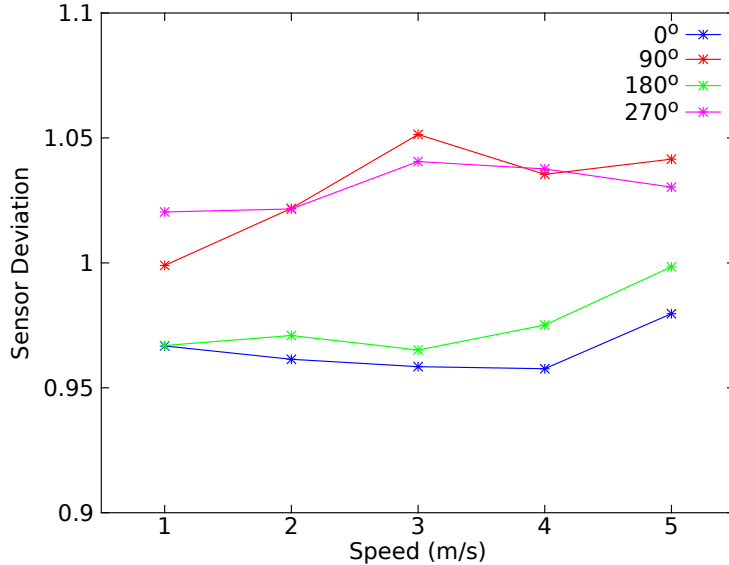


Figure 44: Results for carpet 1 and different orientation of the sensor over the moving direction. Shown are the calibration factors of every single experiment compared to the mean value over all experiments. The deviations around 3 % are homogeneous for each direction (forward and backward) should be corrected by software once implemented. These tests were done with 10-13 mm surface distance.

	Line	Carpet 1	Carpet 2	Carpet 3
$E[squal]$	13.5	89.9	119.1	130.2
$\sigma(squal)$	9.5	6.5	5.9	5.0
$E[shutter]$	6.7	11.2	15.1	17.4
$\sigma(shutter)$	1.2	1.3	1.6	2.8

Table 4: Properties of game field lines vs. the carpet itself. Shown are the mean (E) and the standard deviation (σ) of the surface feature count ($squal$) and the $shutter$ (in μs). The surface feature count can be used as a line indicator where sensor readings should be ignored.

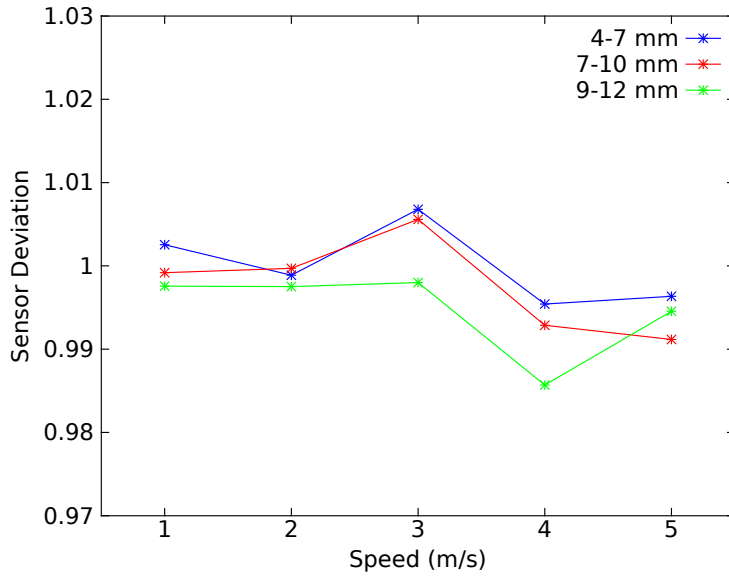


Figure 45: Results for carpet 2 and three distance ranges. Shown are the calibration factors of every single experiment compared to the mean value of 1 m/s. Carpet 2 performs much better than carpet 1. With deviations around 1 % the results are excellent for these distance ranges.

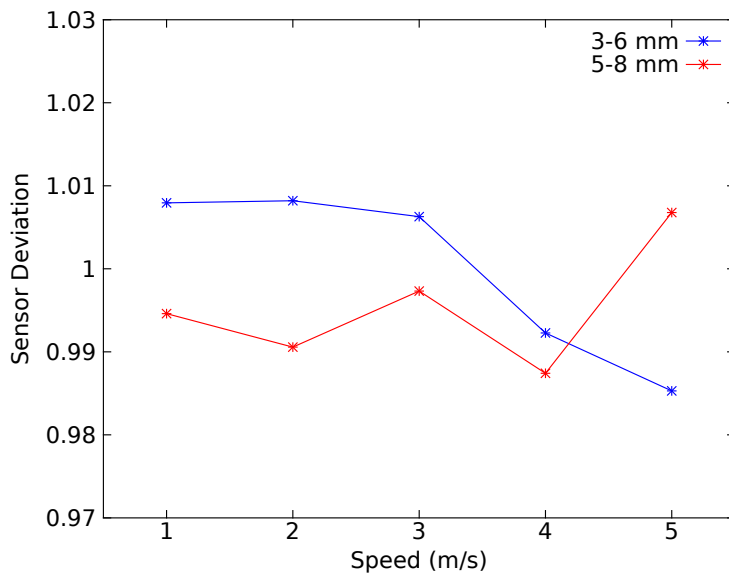


Figure 46: Results for carpet 3 and two distance ranges. Shown are the calibration factors of every single experiment compared to the mean value of 1 m/s. The results are good within 2 % and are considered satisfactory.

6.2.5 Second Series of Experiments

For the publication of the I²MTC-paper a second series of experiments was run to get better results without the influence of the motor. The experiments were repeated on a milling machine where the carpet disc was clamped into the milling head chuck (see Figure 47). The milling head has a very even angular velocity compared to the hand drill motor, so the waveform of the first plots could be eliminated.

In the low speed operating range, due to the fixed gear ratio, only 80, 160 and 245 rpm are available. This corresponds roughly to 1.5, 3 and 4.5 m/s.

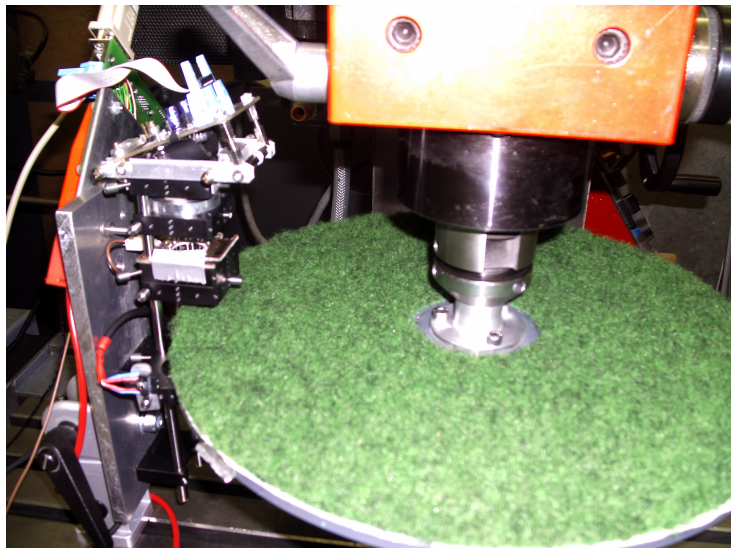


Figure 47: Photo of the sensor mounted on the milling machine. The carpet disc is clamped into the milling head chuck. The sensor itself is mounted on the milling table. The distance to the carpet can be adjusted with the vertical feed of the milling table.

For every carpet one experiment with these three speeds was done. Using a target distance of 5 mm we obtained a sensor bias as shown in Figure 48a. In order to simplify the comparison of different boundary conditions the bias is related to its true value resulting in the measured *relative bias*. In this experiment the sensor signal is sampled with $f_s = 500$ Hz and consequently median filtered ($N = 3$) to remove outliers. It can be seen that, while each carpet leads to a different bias behaviour, the overall relative bias of the odometry sensor is less than 0.6 % over the whole target range of velocities. The associated standard deviations of the odometry readings estimated using $M = 500$ samples, again related to the true velocity, are shown in Figure 48b. Note that while the standard deviation of car-

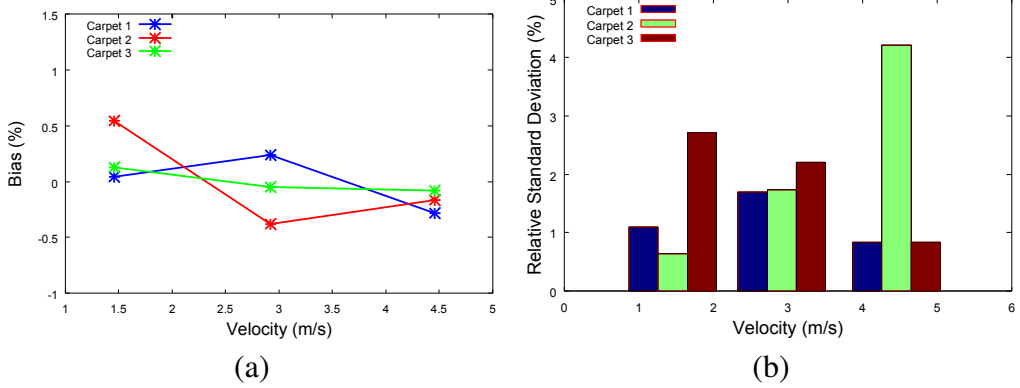


Figure 48: Comparison of the odometry sensor with ground-truth data. (a) Relative bias for different carpets for a constant surface distance of 5 mm. (b) The relative standard deviation of the odometry results are dominated by the optical properties of the carpet used.

pet 2 steadily rises with increasing velocities, the standard deviation of carpet 3 decreases with increasing velocity. These results are caused by the optical properties of the different carpets [23].

For the influence of the surface quality on the bias a series of experiments was run with carpet 1 on a speed of 1.5 m/s. The decreased surface count was induced by decreasing the illumination strength. The results can be seen in Figure 49.

In a last experiment the function of the telecentric optical path design was validated on carpet 1 with a speed of 1.5 m/s. The relative bias of the odometry sensor is investigated for varying surface distances. Figure 50 shows the obtained results augmented by their respective relative standard deviations for a surface distance ranging from 5 mm to 15 mm. A bias of less than 1 % can be observed for a surface distance in the range 5 – 12 mm and the maximum bias is less than 6 % over the whole range of surface distances. The increased bias in this set-up is caused by two effects: First, the optical set-up of the prototype is not perfectly aligned giving raise to telecentricity errors. Second, the surface illumination fails to properly cover the whole range of surface distances [23].

6.3 Conclusion

This work shows that our sensor prototype works sufficiently well on carpet. The added optics make a computer mouse sensor suitable for the RoboCup environment. The bias for every test was below 5 %, which suits the requirements. The

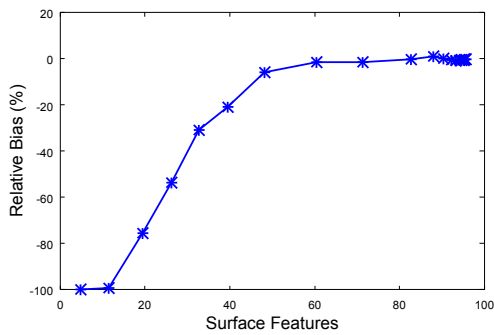


Figure 49: Relative bias introduced by a decreased surface feature count.

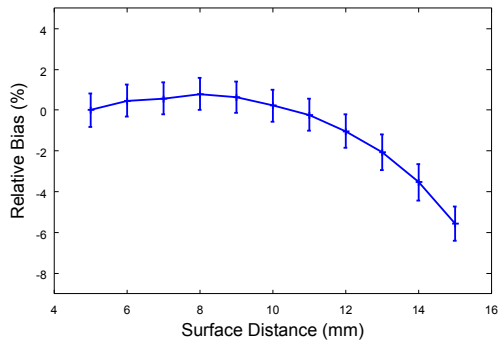


Figure 50: Validation of the telecentric system using a variable surface distance ranging from 5 mm to 15 mm.

surface quality information proved to be a reliable data quality indicator which can be used in our sensor fusion system.

One discovered negative aspect is that the sensor does not work on the game field lines with the current illumination. When using three sensors as intended on the Krikkit3G platform, the six available degrees of freedom should be enough to cover the temporary blackout of one sensor.

The telecentric set-up fulfilled its expectations and the small telecentric errors can be reduced with a more precise optical set-up. The alignment of the telecentric set-up is a rather simple mechanic task and improves the accuracy in a linear way.

7 Outlook

In this section thoughts on continuing this project will be given. The next step will be to design a sensor that can be used in the Krikkit3G. It should go into production in small series from 6 – 20 pieces.

It has to fit into the Krikkit3G space restrictions ($50 \times 50 \times 80 \text{ cm}^3$). In addition, some sort of dust-cleaning mechanism has to be provided for the rather dusty environment on the artificial carpet. Experience shows that after a game the bottom of the robot is covered with an oily film (from the gearboxes and bearings), where green dust from outworn carpet hairs sticks onto. The lens at the bottom has to be protected from this dust.

On the illumination an approach with laser illumination should be tried to get better results on the game field lines through the laser speckle effect. Therefore a strong laser has to be found for this task. The red laser used in the laboratory was not usable on the green carpet because of the poor reflection coefficient of the used wavelength on the green surface. Maybe both LEDs and a laser in parallel or alternating, depending on the current surface, can be used.

When using LEDs more care has to be taken about the cooling, especially in the tighter space constraints of the robot drive.

The successor of our used mouse sensor is available in the meanwhile, the ADNS-90xx. It offers a maximum speed of 5 m/s out of the box. Perhaps the new sensor can save the magnification lens, which would cut down the space requirements and costs of the optical path.

On the microcontroller side the new standard for the “*Mostly Harmless*” RoboCup Team is the ARM architecture, which has to be used on a new sensor. The STM32F103CBT6 chip used in other electronics project of the “*Mostly Harmless*” RoboCup Team offers SPI, CAN and all other needed features.

On the software side an algorithm [3] has to be implemented to compute the three needed dimensions out of 2/4/6 available, depending on the number of sensors which offer reliable data at the moment.



This work, all images and acquired data are published under Creative Commons
Attributions Share-Alike 3.0 Austria²⁵



All source code, if not mentioned otherwise, is licensed under the General Public
Licence (GPL) v3²⁶.

²⁵<http://creativecommons.org/licenses/by-sa/3.0/at/>

²⁶<http://www.gnu.org/licenses/gpl.html>

References

- [1] João Pedro Estilita Antunes. Hardware Architecture and Fast Deployment Methods for Soccer Robots. Master's thesis, Institute for Systems and Robotics, Lisboa, October 2009.
- [2] Avago Technologies. *ADNB-6011 and ADNB-6012 High Performance Laser Mouse Bundles*, May 2008.
- [3] Andrea Bonarini, Matteo Matteucci, and Marcello Restelli. Automatic Error Detection and Reduction for an Odometric Sensor based on Two Optical Mice. In *Proceedings of the 2005 IEEE International Conference on Robotics and Automation*. Department of Electronics and Information, Politecnico di Milano, IEEE, April 2005.
- [4] Georg Brasseur. *Skriptum zur Vorlesung Elektrische Messtechnik*. Institut für Elektrische Meßtechnik und Meßsignalverarbeitung, TU Graz, 2003.
- [5] Xsens Technologies B.V. <http://www.xsens.com> (last accessed 10.10.2010), 2005-2010.
- [6] Canon Inc. *LV-20Z, LV-50Z LASER DOPPLER VELOCITY SENSOR*, 2005.
- [7] MSL Technical Committee. *Middle Size Robot League Rules and Regulations for 2010*. The RoboCup Federation, May 2010.
- [8] CORRSYS-DATRON Sensorsysteme GmbH. *CORREVIT®L-350 Aqua*, October 2008.
- [9] Christian Deutsch. Pfadplanung für einen autonomen mobilen Roboter. Master's thesis, Institut für Regelungstechnik und Automatisierung, Graz, April 2004.
- [10] The RoboCup Federation. <http://www.robocup.org> (last accessed 10.10.2010), 2008.
- [11] Alexander Ferrein, Gerald Steinbauer, Graeme McPhillips, Tim Niemüller, and Anet Potgieter. Team Zadeat 2009 - Team Report, 2009.
- [12] P. Heide, M. Joppich, and R. Schubert. Berührungslose Geschwindigkeitsmessung nach dem Dopplerprinzip mit Ultraschall und Mikrowellen. In *Fachtagung "SENSOREN – Technologie und Anwendung"*. Zentrale Forschung und Entwicklung, Siemens AG, Bad Nauheim, March 1992.
- [13] P. Heide, M. Vossiek, M. Nalezinski, L. Oréans, R. Schubert, and M. Kunert. 24 GHz Short-range Microwave Sensors for Industrial and Vehicular Appli-

- cations. In *Workshop Short Range Radar*. SIEMENS AG, TU Ilmenau, July 1999.
- [14] Honeywell. *HOA1404 Reflective Sensor*, February 1998.
 - [15] Daniel Hrach and Markus Brandner. Optical Side-Slip Angle Measurement for Automotive Applications. In *EDERS2006*, pages 33–39, Munich, June 2006. Texas Instruments.
 - [16] K. Imou, M. Ishida, T. Okamoto, Y. Kaizu, A. Sawamura, and N. Sumida. Ultrasonic Doppler Sensor for Measuring Vehicle Speed in Forward and Reverse Motions Including Low Speed Motions. *the CIGR Journal of Scientific Research and Development*, III(Manuscript PM 01 007), 2001.
 - [17] Infineon Technologies AG, D-81726 Munich, Germany. *XC164CM series Board Manual*, v.1.0 edition, January 2006.
 - [18] H. Jäger. *Experimentalphysik 1*. Institute of Experimental Physics, Graz University of Technology, 2000.
 - [19] Otto Koudelka. *Nachrichtentechnik*. Skriptenreferat der Hochschülerschaft an der TU Graz Ges.m.b.H., 2006.
 - [20] Gerald Krammer. *Intelligente Stromversorgung für einen Roboter*. Graz University of Technology, May 2006. IT-Projekt Elektronik.
 - [21] Gerald Krammer. Elektronisches Gesamtkonzept für einen mobilen Roboter. Master's thesis, Institute for Electronics, Graz University of Technology, Graz, May 2007.
 - [22] Linos Photonics GmbH & Co. KG. *Microbench, Bench and Rail Systems*, 2010.
 - [23] Michael Maier and Markus Brandner. Low-Cost Optical Odometry for Wheeled Mobile Robots. In *Proceedings of the 2011 IEEE International Instrumentation and Measurement Technology Conference - I²MTC 2011*, pages 986–971. IEEE, May 2011.
 - [24] A. Martins, J. Almeida, E. Silva, and J. P. Baptista. Design of the ISepporto Robocup Middle-Size League Robotic Soccer Team: Control, Localisation and Coordination. In *Proceedings of the 10th Mediterranean Conference on Control and Automation - MED2002*. Instituto Superior de Engenharia do Porto, July 2002.
 - [25] Brandstötter Mathias and Dimitris Tselenis. *Maschinenbau im RoboCup, Spielfreies Mecanum-Wheel*. Graz University of Technology, May 2007. Projekt konstruktiv.

- [26] LL.D. Noah Porter, D.D. *Webster's Revised Unabridged Dictionary*. C. & G. Merriam Co. Springfield, Mass., 1913.
- [27] M.Danesh Panah, A.Abdollahi, H.Ostadi, and H.Samani. *Comprehensive Omni-Directional Soccer player Robots*, chapter 18. Advanced Robotic Systems International & Pro Verlag, September 2007.
- [28] Rainer Schuhmann and Thomas Thöniß. Telezentrische Systeme für die optische Meß- und Prüftechnik. *Technisches Messen*, 65(4):131–136, 1998.
- [29] Thomas Thurner, Sebastian. C. Schneider, and Bernhard. G. Zagar. Laser Speckle Strain Measurement and its Application in Material Science. *Technisches Messen*, 70(2):71–78, 2003.
- [30] Chen-Chia Wang, Sudhir B. Trivedi, Feng Jin, Serguei Stepanov, Zhongyang Chen, Jacob Khurgin, Ponciano Rodriguez, and Narasimha S. Prasad. Human Life Signs Detection Using High-Sensitivity Pulsed Laser Vibrometer. *IEEE SENSORS JOURNAL*, 7(9):1370–1376, September 2007.
- [31] Roland Würschum. *Physik moderner Technik*. TU Graz, Institut für Experimentalphysik, 2009.